CrossMark

J. Fluid Mech. (2017), *vol.* 814, *pp.* 452–483. © Cambridge University Press 2017
doi:10.1017/jfm.2017.23

Droplet dynamics and fine-scale structure in a shearless turbulent mixing layer with phase changes

Paul Götzfried[1,†], Bipin Kumar[2], Raymond A. Shaw[3] and Jörg Schumacher[1]

[1]Institut für Thermo- und Fluiddynamik, Postfach 100565, Technische Universität Ilmenau, D-98684 Ilmenau, Germany

[2]Indian Institute of Tropical Meteorology, Dr Homi Bhaba Road, Pashan, Pune 411008, Maharashtra, India

[3]Department of Physics, Michigan Technological University, Houghton, MI 49931, USA

(Received 17 March 2016; revised 21 December 2016; accepted 5 January 2017; first published online 8 February 2017)

Three-dimensional direct numerical simulations of a shearless mixing layer in a small fraction of the cloud–clear air interface are performed to study the response of an ensemble of cloud water droplets to the turbulent entrainment of clear air into a cloud filament. The main goal of this work is to understand how mixing of cloudy and clear air evolves as turbulence and thermodynamics interact through phase changes, and how the cloud droplets respond. In the main simulation case, mixing proceeds between a higher level of turbulence in the cloudy filament and a lower level of turbulence in the clear air environment – the typical shearless mixing layer set-up. Fluid turbulence is driven solely by buoyancy, which incorporates feedbacks from the temperature, the vapour content and the liquid water content fields. Two different variations on the core set of shearless mixing layer simulations are discussed, a simulation in a larger domain and a simulation with the same turbulence level inside the filament and its environment. Overall, it is found that, as evaporation occurs for the droplets that enter subsaturated clear air regions, buoyancy comes to dominate the subsequent evolution of the mixing layer. The buoyancy feedback leads initially to downdraughts at the cloudy–clear air interface and to updraughts in the bulk regions. The strength of the turbulence after initial transients depends on the domain size, showing that the range of scales is an important parameter in the shearless mixing layer set-up. In contrast, the level of turbulence in the clear air is found to have little effect on the evolution of the mixing process. The distributions of cloud water droplet size, supersaturation at the droplet positions and vertical velocity are more sensitive to domain size than to the details of the turbulence profile, suggesting that the evolution of cloud microphysics is more sensitive to large-scale as opposed to small-scale properties of the flow.

Key words: condensation/evaporation, particle/fluid flow, turbulent mixing

† Email address for correspondence: paul.goetzfried@tu-ilmenau.de

https://doi.org/10.1017/jfm.2017.23 Published online by Cambridge University Press

1. Introduction

Turbulent entrainment and subsequent mixing are observed in many processes in nature and technology, and occur when flows with different levels of turbulence are brought together to form a thin interface (da Silva *et al.* 2014). For turbulent clouds in the atmosphere, not only different turbulent levels, but also different phases of water, water vapour, water droplets and ice crystals coexist. The entrainment and mixing of dry clear air with cloudy moist air to a large extent determines the overall lifetime and shape of clouds (Blyth 1993; Shaw 2003; Stevens & Bony 2013). Mixing at the cloud boundary as well as inside the cloud occurs over a broad range of spatial scales, reaching from the smallest eddies at the size of the Kolmogorov length ($\eta_K \sim 1$ mm) to the outer scale ($L \sim 100$ m) and beyond. The associated time scales vary between Kolmogorov times ($\tau_K \sim 10$ ms) up to the lifetime of the cloud ($T_L \sim 1$ h).

The range of scales involved in the dynamics of a turbulent cloud cannot be covered by fully resolved numerical simulations (Atkinson & Zhang 1996). They require studies that parametrize the action of the smaller turbulent eddies and the cloud microphysics in subgrid-scale models or other parametrizations (Bodenschatz *et al.* 2010). The complexity of the multiscale dynamics is further enhanced at the cloud boundary where cloudy air with cloud water droplets (and ice crystals) and clear air form a complex-shaped interface. Additional coupling of the turbulent fields to the nonlinear thermodynamics of phase changes and droplet–droplet interactions results in a setting that has multiple feedbacks. Evaporation of the droplets causes a local evaporative cooling, which affects fluid motion via buoyancy. This generates a fluid subsiding motion at the cloud–clear air interface (see e.g. Austin *et al.* 1985; Heus & Jonker 2008; Abma, Heus & Mellado 2014). The strong shearing motion in turn affects the droplet advection and thus their evaporation and interaction with the small-scale turbulence.

Direct numerical simulations (DNS), which resolve the turbulence down to the smallest eddy size, allow us to study some of these aspects in canonical and idealized settings and to disentangle the multiple feedbacks between small-scale turbulence and droplet dynamics. One such configuration that can be considered as a paradigm for the turbulence at the edge of an atmospheric cloud is the shearless or shear-free mixing layer – one of the simplest set-ups of inhomogeneous turbulence. Such a layer is formed when two homogeneous and turbulent subdomains with different mean kinetic energies are brought together. This configuration has been studied in experiments starting with Gilbert (1980) and Veeravalli & Warhaft (1989) as well as in DNS by Briggs, Ferziger & Koseff (1996), Knaepen, Debliquy & Carati (2004) or Tordella & Iovieno (2006, 2011). Lagrangian experiments that investigated the velocity gradients at the entrainment interface were reported by Holzner *et al.* (2008). In a shearless mixing layer, the two subdomains have no relative velocity with respect to each other. The triggered entrainment results in a broadening of the initially thin interface layer that separates the two subdomains.

An important step towards a deeper understanding of the mixing in clouds by means of shearless mixing layers was undertaken by Gerashchenko, Good & Warhaft (2011) and Good, Gerashchenko & Warhaft (2012) using laboratory experiments followed by Ireland & Collins (2012) using DNS. The focus of both studies was the dynamics of inertial particles at the turbulence–turbulence interface (TTI). Previous studies by Tordella & Iovieno (2011) revealed strong intermittency, which arises from the turbulent transport across the interface between higher- and lower-level turbulence. Both studies did not consider phase changes and thus neglected latent heat release during condensation and evaporative cooling. The studies showed

https://doi.org/10.1017/jfm.2017.23 Published online by Cambridge University Press

however that particle inertia can contribute to the mixing process, but notably for the turbulent–non-turbulent interface (TNI) that entrainment of particles into clear air is strongly dominated by the large scales of the flow. We keep this suggestion of the importance of large scales in mind in this work.

Several aspects of the droplet growth have been considered in Eulerian and Euler–Lagrangian numerical studies in the bulk of a cloud. Growth by condensation, allowing the humidity to fluctuate due to droplet inertia and turbulent mixing, was studied for example by Vaillancourt, Yau & Grabowski (2001), Andrejczuk *et al.* (2006, 2009), Lanotte, Seminara & Toschi (2009) and Gotoh, Suehiro & Saito (2016).

Growth by collision and coalescence, again in the bulk of a turbulent cumulus cloud, was investigated for example by Onishi, Matsuda & Takahashi (2015) and Sardina *et al.* (2015) (for a review see also Grabowski & Wang (2013)). They explore the extent to which turbulence and relative velocity between inertial droplets change the collision efficiency in a local fluid environment. As a result, collision and coalescence rates increase and broaden the particle size distribution. These processes gain an increasing relevance as the mean droplet radius grows significantly beyond the radii that are considered in our study. Recently Perrin & Jonker (2015) addressed the Lagrangian droplet dynamics in the cloud–clear air interface. They included simple collision and coalescence models. A broadening of the droplet size distribution is found to be a joint effect of evaporation, decoupling due to gravity and coalescence.

Our former numerical studies in a similar context (Kumar *et al.* 2012; Kumar, Schumacher & Shaw 2013, 2014) investigated the turbulent mixing in fluid turbulence with a uniform level of fluid turbulence inside and outside the cloud. Here, we modify the initial condition in such a way that we have a higher level of fluid turbulence inside the cloud slab and a lower level of fluid turbulence in the clear air region next to the filament. Higher and lower level refer to the root mean square magnitude of the velocity components and the mean amplitude of the kinetic energy dissipation rate. This is a further step towards reproducing more realistic conditions at the cloud boundary in DNS. Our ansatz is supported by high-resolution field measurements of trade-wind cumuli in the CARRIBA (CARRIBA stands for Cloud, Aerosol, Radiation and tuRbulence in the trade wInd regime over BArbados) project over Barbados (Siebert *et al.* 2013; Katzwinkel *et al.* 2014). These measurements were conducted with a helicopter-based cloud turbulence observation system, which measures for example velocity, temperature, droplet and aerosol concentrations simultaneously (see Siebert *et al.* 2006 for more details). They resolved the variation of the turbulent fluctuations of all involved fields across the cloud boundary down to a resolution of approximately 20 cm. We adjust the mean kinetic energy dissipation rates and velocity fluctuations in our DNS accordingly.

In this work, we study the initial stage of the entrainment of cloudy moist air into clear dry environmental air as present at the edge of a cloud using highly resolved three-dimensional pseudospectral DNS without any parametrizations of the small-scale turbulence and cloud microphysics. We investigate the global turbulent mixing dynamics, which includes full thermodynamic coupling to the dispersed droplets that are able to grow or evaporate depending on local conditions. Specifically, we examine the nonlinear thermodynamic feedback on the flow via the buoyancy and strength of lateral entrainment, and, ultimately, the imprint left on the cloud droplet size distribution as a result of the mixing. Droplets are treated as Lagrangian inertial point particles (see also Toschi & Bodenschatz 2009 for a review). The pseudospectral simulations also allow us to relate the phase changes at the interface to the small-scale shear and vorticity production in this region of a cloud.

https://doi.org/10.1017/jfm.2017.23 Published online by Cambridge University Press

In addition to the velocity, we include temperature, vapour and liquid water contents as well as their multiple couplings via buoyancy, latent heat release and supersaturation in our study. In order to maintain focus, the initial stage of the mixing at the cloud edge without droplet collisions and coalescence is considered (see also § 2.2 for further discussion). Ice – the third possible phase in an atmospheric cloud – is excluded in this study. In the present work, we focus on two possible aspects of the flow that may influence these processes: the effect of the domain size on the mixing process, which effectively allows the range of contributing spatial and temporal scales to be varied; and the effect of the turbulence profile across the mixing layer.

Our initial configuration differs also in a further aspect from previous studies. It exhibits a negative buoyancy inside the cloud and thus corresponds to the particular case of a dissolving cloud as discussed by Katzwinkel *et al.* (2014). The evaporative cooling leads to an increase of buoyancy (see also Malinowski *et al.* 2008) and generates a transient amplification of the (otherwise freely decaying) turbulence accompanied by the generation of a shear layer, which would correspond to the subsiding shell on a larger scale. In this setting, we investigate the interaction of the small-scale vortices and shear layers with the droplet dynamics. The domain size for our largest DNS provides already a significant level of turbulence and thus a scale separation towards the inhomogeneous mixing regime which is found to be dominant in real cloud turbulence (Beals *et al.* 2015).

The outline of the paper is as follows. In the next section, we describe our numerical model and the set-up of the initial field. In § 3 we present results of the different simulation runs. This section contains our investigations of the global dynamics, plane-averaged statistics of buoyancy and buoyancy fluxes as well as on the growth of the mixing layer and the production of small-scale velocity gradients at the interface. Section 4 describes the droplet response to the mixing. Here, probability density functions of temperature, droplet radius and supersaturation at droplet position are discussed. Furthermore, the joint statistics of temperature and vapour content and the dynamics of individual droplet trajectories are presented. Finally, we conclude with a summary and an outlook for future work.

2. Numerical model and initial set-up

2.1. *Equations of motion for the turbulence fields*

We combine the Eulerian description of the turbulent velocity, temperature and vapour content fields with the Lagrangian description of the ensemble of cloud water droplets. Condensation rate, liquid water content and local supersaturation determine the diffusional growth of the individual cloud water droplets. Typical cloud droplet concentrations of the order of 10^2 cm^{-3} result in approximately 10–100 million individual droplets. They are treated as inertial point particles with Stokes drag and gravitational settling. We monitor their position, their velocity and the droplet radius.

Turbulence is simulated in a Cartesian slab volume with a maximum size of 2 m $\times$ 1 m $\times$ 1 m. The Kolmogorov scale of $\eta_K \approx 1$ mm is chosen here in all runs, which is typical for cumulus clouds (Lehmann, Siebert & Shaw 2009). Recall that the Kolmogorov scale defines the smallest vortices in the turbulent cloud, the end of the turbulent inertial cascade.

The turbulent velocity field $u_i(x_j, t)$, the temperature field $T(x_j, t)$ and the pressure field $p(x_j, t)$ are the fields necessary for the description of dry turbulent convection. In the following, x_i, x_j or $x_k = (x, y, z)$. We use the Einstein sum convention for indices i, j, k. In the case of phase changes during the mixing process, we have to

https://doi.org/10.1017/jfm.2017.23 Published online by Cambridge University Press

add two mixing ratios, the vapour mixing ratio field $q_v(x_j, t) = \rho_v/\rho_d$ and the liquid water mixing ratio field $q_l(x_j, t) = \rho_l/\rho_d$, since phase changes are present. Here, ρ_d, ρ_v and ρ_l are mass densities of dry air and water vapour, and liquid water content, respectively. The Eulerian equations in the Boussinesq approximation are then given by

$$\frac{\partial u_i}{\partial x_i} = 0, \tag{2.1}$$

$$\frac{\partial u_i}{\partial t} + u_j \frac{\partial u_i}{\partial x_j} = -\frac{1}{\rho_0}\frac{\partial p}{\partial x_i} + \nu \frac{\partial^2 u_i}{\partial x_j^2} + B\delta_{zi}, \tag{2.2}$$

$$\frac{\partial T}{\partial t} + u_j \frac{\partial T}{\partial x_j} = \kappa \frac{\partial^2 T}{\partial x_j^2} + \frac{L}{c_p} C_d, \tag{2.3}$$

$$\frac{\partial q_v}{\partial t} + u_j \frac{\partial q_v}{\partial x_j} = D \frac{\partial^2 q_v}{\partial x_j^2} - C_d. \tag{2.4}$$

The buoyancy field B in (2.2) depends on three fields, the temperature T, the vapour mixing ratio q_v and the liquid water mixing ratio q_l, respectively. It is given by

$$B = g\left[\frac{T'}{\langle T\rangle} + \varepsilon q_v' - q_l\right]. \tag{2.5}$$

Here, ν is the kinematic viscosity of air and g is the gravitational acceleration. The quantity ρ_0 is the reference value for dry air mass and $\varepsilon = 0.608$. The temperature fluctuations are given by

$$T'(x_j, t) = T(x_j, t) - \langle T(t)\rangle, \tag{2.6}$$

and the vapour mixing ratio fluctuations by

$$q_v'(x_j, t) = q_v(x_j, t) - \langle q_v(t)\rangle, \tag{2.7}$$

with $\langle\cdot\rangle$ being a volume average. The quantity c_p is the specific heat at constant pressure, L is the latent heat, κ is the diffusivity of the temperature, and D is the diffusivity of the vapour mixing ratio. Here, $\kappa \approx D$.

2.2. *Lagrangian model for cloud water droplets*

In our numerical approach, the liquid water mixing ratio q_l and the condensation rate C_d are calculated in the Lagrangian frame of reference since particles are advected in the turbulent flow. Their properties have to be 'translated' into the Eulerian frame of reference for use in (2.3) and (2.4). In turn, flow field properties have to be determined at the droplet position in order to advance the Lagrangian equations as visible in (2.8)–(2.11) below.

Since the Stokes numbers and the mass loading are small, the feedback of the droplets on the flow is only considered as the drag of liquid mass on the flow, which is included by the term $-gq_l$ in the buoyancy in (2.5). Additional terms in the equation of motion that exist even for low Reynolds number include Faxen term, added mass, pressure gradient, and Basset history forces (see Crowe, Sommerfeld & Tsuji 1998, § 4.3). For our simulation conditions, the forces are estimated to have the following orders of magnitude relative to Stokes drag: Faxen 10^{-5}, added mass 10^{-6}, pressure gradient 10^{-3}, Basset history 10^{-2}. This is consistent with the conclusion from other works that Stokes drag is the dominant contribution for heavy particles

https://doi.org/10.1017/jfm.2017.23 Published online by Cambridge University Press

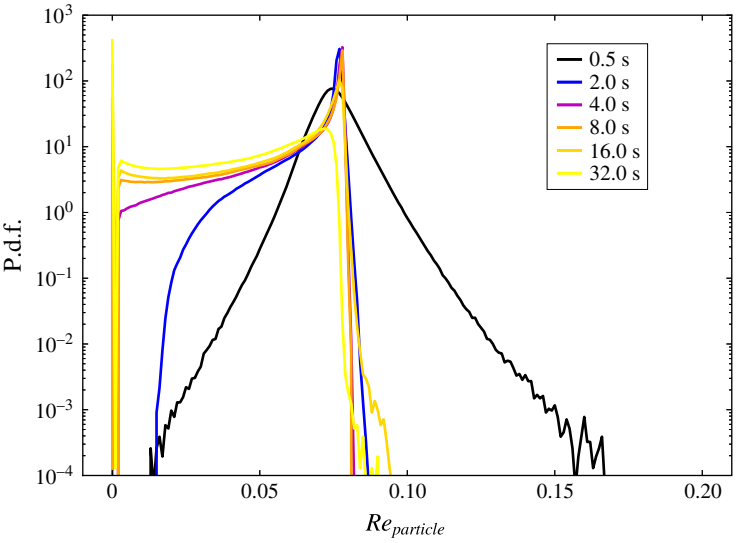


FIGURE 1. (Colour online) Probability density function of the particle Reynolds number for different times of the mixing process. Data are obtained from simulation run TNIa, which is displayed in table 1.

in turbulent gas flows for a density ratio of $\sim 10^{-3}$ (Shaw 2003; Bergougnoux *et al.* 2014; Olivieri *et al.* 2014).

The Lagrangian evolution of each of the N_d cloud droplets is described by the following set of equations:

$$\frac{\mathrm{d}X_i}{\mathrm{d}t} = V_i(X_j, t), \tag{2.8}$$

$$\frac{\mathrm{d}V_i}{\mathrm{d}t} = \frac{1}{\tau_p}[u_i(X_j, t) - V_i(X_j, t)] + g_i. \tag{2.9}$$

Here, X_i is the space coordinate vector at each particle position and V_i its velocity, which differs from the velocity of the air, u_i, at the droplet position. Gravitational acceleration is $g_i = -g\delta_{zi}$ and particle response time (or Stokes time) is τ_p. The definition of τ_p follows later in the text. The particle response time is adjusted to the droplet radius in the dynamical evolution. Here we use the linear Stokes drag model, since the particle Reynolds number

$$Re_{particle} = \frac{|u_i(X_j, t) - V_i(X_j, t)|d}{\nu}, \tag{2.10}$$

with droplet diameter d and the absolute velocity difference $|u_i(X_j, t) - V_i(X_j, t)|$, is always smaller than 0.1 (see figure 1). According to investigations of Bergougnoux *et al.* (2014) nonlinear corrections can therefore be excluded for small Stokes numbers $St < 0.1$. The droplet radius growth by vapour diffusion is described by the following equation (see e.g. Kumar *et al.* 2013 and references therein),

$$r(X_i, t)\frac{\mathrm{d}r(X_i, t)}{\mathrm{d}t} = KS(X_i, t), \tag{2.11}$$

where K is a constant. Equations (2.8)–(2.11) are coupled to equations (2.1)–(2.5) and are simultaneously integrated forward in time. The Lagrangian equations are still

https://doi.org/10.1017/jfm.2017.23 Published online by Cambridge University Press

Run	$N_x \times N_y \times N_z$	$L_x \times L_y \times L_z$	k_2/k_1	Re	a (mm)	N_d	t_{total} (s)
TNIa	1024×512^2	1.0 m $\times$ 0.5 m^2	0.01	9000	1	1.5×10^7	83
TTIa	1024×512^2	1.0 m $\times$ 0.5 m^2	1.0	9000	1	1.5×10^7	83
TNIb	2048×1024^2	2.0 m $\times$ 1.0 m^2	0.01	27 000	1	1.2×10^8	41

TABLE 1. Parameters of the different direct simulation runs. We denote the run with the same turbulent kinetic energy (TKE) in- and outside the cloud as TTI for turbulent–turbulent interface, the runs with different levels as TNI for turbulent–non-turbulent interface. The second column displays the number of grid points covering the whole simulation domain, the third column the size of the rectangular box. The fourth column stands for the approximate ratio of the TKE in the clear air half (k_2) and the cloudy half (k_1). The Reynolds number is given by $Re = u_{rms}L_x/\nu$. The Kolmogorov scale η_K will match the uniform grid spacing a in all cases. In the penultimate column N_d is the total number of droplets. The total time span t_{total} of the integration is given in the last column.

solved even for droplets that are fully evaporated. Particles with radius $r \leqslant 0.5$ μm are considered to have very small inertia and are handled as passive Lagrangian tracers. Therefore the Lagrangian dynamics simplify to only (2.8) with $\mathrm{d}X_i/\mathrm{d}t = u_i(X_j, t)$ excluding (2.9). Throughout the paper all Lagrangian statistics include particles with zero radius, unless otherwise noted in the text.

The supersaturation field S is determined from the vapour mixing ratio and is given by

$$S(X_i, t) = \frac{q_v(X_i, t)}{q_{vs}(T)} - 1. \tag{2.12}$$

The saturation vapour mixing ratio $q_{vs}(T)$ has to be determined from the temperature as a solution of the Clausius–Clapeyron equation. It is given by

$$q_{vs}(T) = \frac{e_s(T)}{R_v \rho_0 T}, \tag{2.13}$$

with the specific gas constant for vapour R_v. The saturation pressure e_s is given by $e_s(T) = c_1 \exp(-c_2/T)$ (see Rogers & Yau 1989 for more details). Here, c_1 and c_2 are constants, which are listed in table 2.

Practically, for the conditions of this study, the droplet collision rate is expected to be negligible over the time we have simulated. Initially the droplets are all of a single size, so the primary contributions to collision rate are shear and inertial effects (see e.g. Shaw 2003). As the distribution becomes broader, differential sedimentation becomes dominant. The time scale for a collision due to differential sedimentation scales as $\tau_{1,2} \sim (n\pi(d_1 + d_2)^2|v_{t,1} - v_{t,2}|\epsilon_{1,2})^{-1}$, where subscripts 1 and 2 represent droplets of two sizes, n is droplet number density, d is droplet diameter, v_t is terminal speed, and ϵ is the collision efficiency (Rogers & Yau 1989). For typical droplet sizes and best estimates of ϵ, this time is of order 1–10 h, thus much greater than the large-eddy turnover time. Furthermore, turbulent enhancements of the collision rate are less than a factor of 2 for the simulated conditions (Grabowski & Wang 2013).

2.3. *Evaluation of condensation rate*

The liquid water mixing ratio is calculated by summing up the liquid water mass of the droplets in each grid cell. To close the coupled system of Eulerian and Lagrangian

https://doi.org/10.1017/jfm.2017.23 Published online by Cambridge University Press

Quantity	Symbol	Unit	Value
Latent heat of evaporation	L	J kg^{-1}	2.5×10^6
Heat capacity at constant pressure	c_p	J kg^{-1} K^{-1}	1005
First constant for $q_{vs}(T)$	c_1	Pa	2.53×10^{11}
Second constant for $q_{vs}(T)$	c_2	K	5420
Density of the atmosphere	ρ_0	kg m^{-3}	1.06
Gas constant for water vapour	R_v	J kg^{-1} K^{-1}	461.5
Vapour diffusivity	D	m^2 s^{-1}	2.52×10^{-5}
Volume fraction of liquid	χ		0.5
Conductivity	k	J m^{-1} s^{-1} K^{-1}	2.55×10^{-2}
Liquid water density	ρ_l	kg m^{-3}	10^3
Initial droplet radius	R_0	μm	16
Cloud number density	n_d	cm^{-3}	115
Environment saturation mixing ratio	$q_{vs,e} = q_{vs}(T_e)$		1.63×10^{-2}
Cloud slab saturation mixing ratio	$q_{vs,c} = q_{vs}(T_c)$		1.54×10^{-2}
Initial environment mixing ratio	$q_{v,e} = q_v(T_e)$		1.0×10^{-2}
Initial cloud slab mixing ratio	$q_{v,c} = q_v(T_c)$		1.57×10^{-2}
Environment temperature	T_e	K	293
Cloud slab temperature	T_c	K	292
Environment saturation pressure	$e_{s,e} = e_s(T_e)$	Pa	2341
Modified vapour diffusivity	D'	m^2 s^{-1}	6.74×10^{-6}
Constant in (2.11)	K	m^2 s^{-1}	1.17×10^{-10}
Stokes number for atmospheric condition	$St = \tau_p/\tau_\eta$		2.92×10^{-2}
Normalized settling velocity	$W = g\tau_p/v_\eta$		3.17

TABLE 2. List of constants, reference values and initial simulation parameters. Particle time scale τ_p and Kolmogorov time scale τ_η are defined in table 3. The Kolmogorov velocity is defined as $v_\eta = (\langle\epsilon\rangle\nu)^{1/4}$.

equations (2.1)–(2.12), we determine the condensation rate field $C_d(x_i, t)$ by

$$C_d(x_i, t) = \frac{1}{m_a}\frac{\mathrm{d}m_l(x_i, t)}{\mathrm{d}t} = \frac{4\pi\rho_l K}{\rho_0 a^3}\sum_{\beta=1}^{\Delta} S(X_i^\beta, t) r(X_i^\beta, t). \tag{2.14}$$

Here, m_a is the mass of air per grid cell, m_l is the mass of liquid per grid cell and the sum from $\beta = 1$ to Δ collects the droplets inside each grid cell of size a^3 surrounding the spatial point x_i (see also Vaillancourt *et al.* 2001). The mass of liquid m_l is the sum over all droplets, which are spheres. Together with (2.11) for the change of the droplet radius, this results in the final expression for the condensation rate to the right. The transmission of the Eulerian field values at grid positions to the enclosed droplet position is done by trilinear interpolation. The inverse procedure is necessary for the calculation of the condensation rate, which is evaluated first at the droplet position and then redistributed to the nearest eight grid vertices.

2.4. *Numerical method*

The DNS applies a high-resolution pseudospectral method based on a Fourier series expansion of all Eulerian turbulence fields (Schumacher, Sreenivasan & Yakhot 2007). Spectral methods converge exponentially fast and provide an accurate approximation of the strongly fluctuating gradients of the turbulent fields at the smallest scales. The simulation domain consists of an equally spaced mesh grid

https://doi.org/10.1017/jfm.2017.23 Published online by Cambridge University Press

Quantity	Definition	TNIa	TTIa	TNIb
Kolmogorov time (ms)	$\tau_\eta = (\nu/\langle\epsilon_B\rangle)^{1/2}$	122	122	122
Initial particle response time (ms)	$\tau_p = 2\rho_l R_0^2/9\rho_0\nu$	3.6	3.6	3.6
Initial phase relaxation time (s)	$\tau_{ph} = (4\pi D' n_d R_0)^{-1}$	6.4	6.4	6.4
Initial large-eddy turnover time (s)	$T_{L,0} = L_x/\sqrt{2k_0}$	4.5	1.3	8.0
Large-eddy turnover time, A (s)	$T_{L,A} = L_x/\sqrt{2k_A}$	23.9	27.0	36.1
Large-eddy turnover time, B (s)	$T_{L,B} = L_x/\sqrt{2k_B}$	7.7	9.1	10.3
Droplet evaporation time (s)	$\tau_{ev} = -R_0^2/2KS$	2.7	2.7	2.7

TABLE 3. List of important time scales in the mixing process. Times A and B are indicated as the first two vertical dotted lines in figure 3(a,b). Quantities k_0, k_A, k_B and $\langle\epsilon_B\rangle$ refer to the values of the quantities at $t = 0$ s, $t \approx 4$ s and $t \approx 15$ s for cases TNIa and TTIa. Quantities k_B and $\langle\epsilon_B\rangle$ are taken at time $t \approx 24$ s for TNIb. In all cases $\langle\epsilon_B\rangle \approx 10$ cm^2 s^{-3}, which is a typical atmospheric value. Time scale $T_{L,B}$ is chosen as a typical eddy turnover time.

with up to $2048 \times 1024 \times 1024$ grid points for a box size $L_x \times L_y \times L_z$ of up to 2 m $\times$ 1 m $\times$ 1 m. We apply periodic boundary conditions in all three directions. A second-order time stepping with a predictor–corrector scheme is used. Our spectral resolution always satisfies $k_{max}\eta_K \gtrsim 3$, such that the trilinear interpolation in the Lagrangian model is expected to be sufficient.

The simulation program is parallelized in two dimensions using the Message Passing Interface and a two-dimensional domain decomposition of the whole volume into slabs. Table 1 shows all simulation runs and lists some important parameters. Throughout the whole paper, we will name the case with equal turbulence level the turbulent–turbulent interface case (TTI), the case with a lower turbulence level in the clear air region outside the cloud the turbulent–non-turbulent case (TNI). The latter corresponds to the shearless mixing layer. Cases TTIa and TNIa will be directly compared. Run TNIb represents the shearless mixing case with a larger simulation domain, which allows us to explore the importance of the range of scales.

The production runs were conducted on up to 4096 processor cores. The most computationally expensive job TNIb took 18 days for 85 000 time steps to be completed. Jobs TNIa and TTIa were run on 512 cores and took approximately 6 days for 120 000 time steps. The particle tracking is also fully parallelized. Particle data are exchanged between processors when the droplet leaves the subdomain which is associated with a processor. For the biggest simulations, particle tracking takes approximately 15 % of the total time of an integration time step. We continue to track droplets even when they are fully evaporated, although these droplets no longer affect the dynamics.

2.5. *Initial shearless mixing layer configuration*

The velocity field is initialized in wavenumber space by random Fourier amplitudes with a predefined energy spectrum (Rogallo 1981). This results in integral length scales of the initial configuration that are smaller than L_y ($= L_z$). For example, $L(t = 0) \approx 11$ cm for run TNIa. For the cases of a shearless mixing layer (TNI), the velocity field $u_i(x_j)$ is transformed to physical space and rescaled by a mixing function $g(x)$ as used by Tordella & Iovieno (2011):

$$u_i(x_j) = g(x)u_i^{(1)}(x_j) + (1 - g(x))u_i^{(2)}(x_j), \tag{2.15}$$

https://doi.org/10.1017/jfm.2017.23 Published online by Cambridge University Press

with

$$g(x) = \frac{1}{2}\left[1 + \tanh\left(\frac{cx}{L_x}\right)\tanh\left(\frac{c(x - L_x/2)}{L_x}\right)\tanh\left(\frac{c(x - L_x)}{L_x}\right)\right]. \tag{2.16}$$

Indices 1 and 2 correspond to V_1 and V_2, respectively. The ratio of turbulence levels as displayed in table 1 follows from

$$\frac{k_2}{k_1} = \frac{\langle u_i^2(t=0)\rangle_{V_2}}{\langle u_i^2(t=0)\rangle_{V_1}}. \tag{2.17}$$

The blending factor c in the scaling function $g(x)$ determines the width of the mixing layer. We take the same value of $c = 50$ such that the initial interface layer occupies $L_x/50$. Incompressibility is re-established in Fourier space by projection

$$\Pi: \quad \widehat{u}_i(\ell_x, \ell_y, \ell_z) \to \left(\delta_{ij} - \frac{\ell_i \ell_j}{\ell^2}\right)\widehat{u}_j(\ell_x, \ell_y, \ell_z), \tag{2.18}$$

which satisfies $\ell_j \widehat{u}_j(\ell_x, \ell_y, \ell_z) = 0$ with ℓ_x, ℓ_y and ℓ_z being the wavenumbers.

The vapour mixing ratio and temperature fields, $q_v(x_i, t=0)$ and $T(x_i, t=0)$, are rescaled with the same function as the velocity. Amplitudes are matched to values obtained in the CARRIBA experiments. Details are given in table 2. The profiles are chosen such that the contributions of temperature and vapour content compensate each other in the buoyancy B in (2.5). Once all Eulerian fields are set up, we relax the velocity components in a few integration time steps. The final negative buoyancy is due to the additional liquid water content in the form of the initially monodisperse droplets which are seeded randomly in V_1.

Figure 2 displays the initial configuration for cases TNI and TTI. The saturation vapour mixing ratio is marked as a dashed line in figure 2(*a*) corresponding to (2.13). The vapour and temperature profiles are matched to the CARRIBA measurement data with a humidity of approximately 60 % in the clear air region. The temperature jumps by 1 K across the interface. Note that we take a lower temperature in the cloud compared to the environment. As already stated in the introduction, the shearless mixing layer configuration in our study represents a typical situation at the side of a warm dissolving cumulus cloud.

We take the initial set-up in such a way that liquid water is completely transformed into vapour, i.e. all droplets evaporate eventually. To estimate the necessary amplitudes, we start with a set of equations that describe the mixing of two parcels as suggested by Gerber, Frick & Jensen (2008). The equations are derived from the conservation of liquid potential temperature $\theta_l = T - (L/c_p)q_l$ and total water mass $q_{total} = q_v + q_l$ and are given by

$$q_l + q_{vs}(T) = \chi[q_{lc} + q_{vsc}(T_c)] + (1-\chi)q_{ve}, \tag{2.19}$$

$$T - \frac{L}{c_p}q_l = \chi\left(T_c - \frac{L}{c_p}q_{lc}\right) + (1-\chi)T_e. \tag{2.20}$$

They are based on the idea that parcels of air with liquid potential temperature and total water mixing ratio mix linearly. Therefore, the left-hand side represents the state after the mixing of the two parcels and the right-hand side represents the individual parcels, which differ by the mixing fraction χ and $1-\chi$. Here, the initial liquid water

https://doi.org/10.1017/jfm.2017.23 Published online by Cambridge University Press

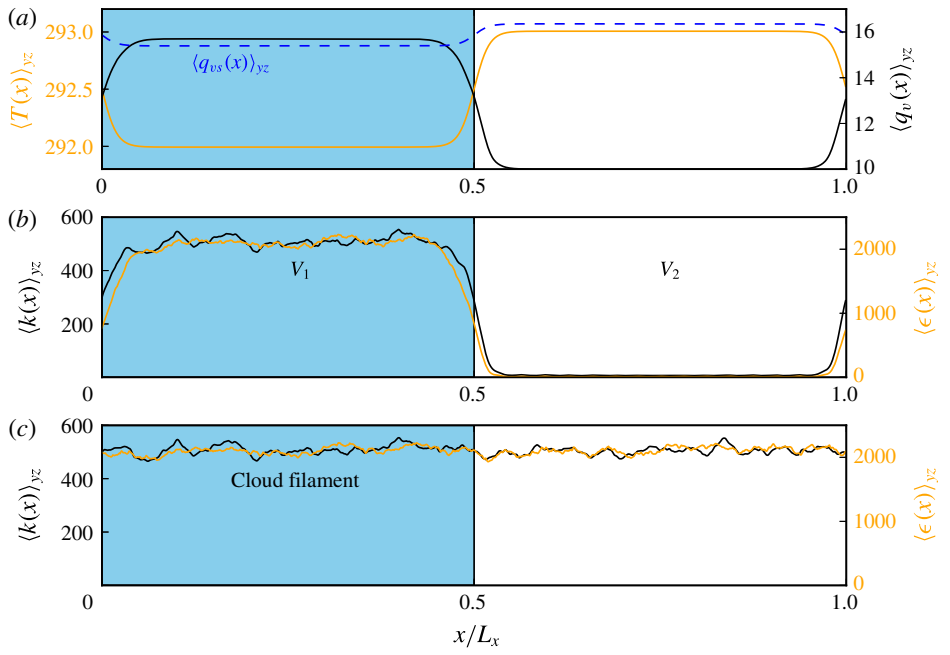


FIGURE 2. (Colour online) Initial configurations of the DNS. The slab is divided into a cloudy half-box V_1 and a clear air half-box V_2. We display initial profiles of the two configurations discussed in the work. A case with a very low level of flow turbulence outside the cloud filament (TNI) is shown in (*b*) and a case with the same turbulence level (TTI) in- and outside the cloud is shown in (*c*). (*a*) Profiles of water vapour mixing ratio $q_v(x, t=0)$ (black/dark solid line), the temperature $T(x, t=0)$ (orange/light solid line) and saturation vapour mixing ratio $q_{vs}(x, t=0)$ (blue/dark dashed line). These profiles are the same for TNI and TTI. (*b*) Turbulent kinetic energy (TKE) (black/dark solid line) and kinetic energy dissipation rate (orange/light solid line) averaged in y–z planes at $t=0$ for TNI. (*c*) Same quantities as in panel (*b*) for the case TTI. Temperature T is measured in K, vapour mixing ratio q_v in g kg^{-1}, TKE k in cm^2 s^{-2} and kinetic energy dissipation rate ϵ in cm^2 s^{-3}.

mixing ratio inside the cloud q_{lc} and the final temperature at the end of the mixing process are the unknowns. We assume that the final liquid water mixing ratio $q_l = 0$. The other variables are the cloud volume fraction χ, the vapour mixing ratio q_{ve} and temperature T_e in the environment V_2. The vapour mixing ratio q_{vc} and temperature T_c are the values in the cloudy subvolume V_1. Solving the equations with N_d from table 1 and R_0 from table 2 results in a temperature of $T_\infty = 290.2$ K at the end of the mixing process.

3. Evolution of the mixing process

3.1. *Global volume-averaged quantities*

Our simulation runs decay freely without additional body forces that enforce a statistically stationary regime. The feedback by the buoyancy is the only term that can amplify the fluid motion transiently. Therefore, the mixing as a whole is a transient process that cannot be characterized by a single set of characteristic time scales as statistically stationary turbulence. We are interested in the time evolution of

https://doi.org/10.1017/jfm.2017.23 Published online by Cambridge University Press

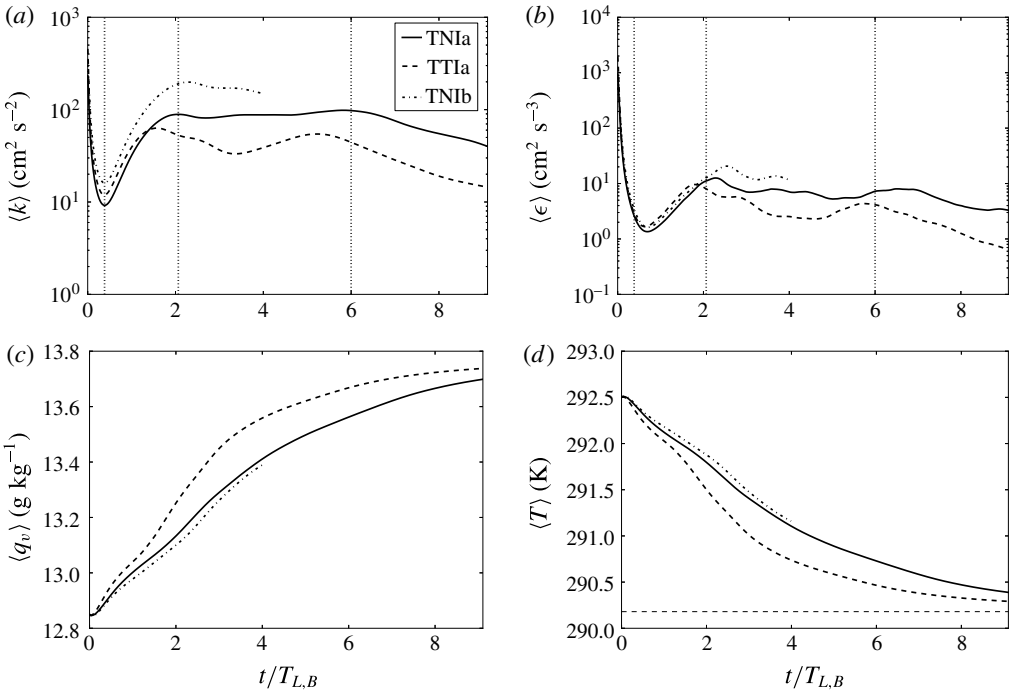


FIGURE 3. Evolution of different volume averages in the course of the decaying turbulence runs: (*a*) mean TKE k; (*b*) mean kinetic energy dissipation rate $\langle \epsilon \rangle$: (*c*) mean vapour mixing ratio $\langle q_v \rangle$; and (*d*) mean temperature $\langle T \rangle$. Temperature T_∞ is indicated as a horizontal dashed line. Time is given in units of a large-scale eddy turnover time $T_{L,B}$, which is listed in table 3. The approximate extension of the four evolution stages is indicated by vertical dotted lines in the upper panels.

the turbulent kinetic energy (TKE), k, and the mean squares of the temperature, k_T, and the vapour fluctuations, k_q, respectively, given by

$$k(t) = \tfrac{1}{2}\langle u_i^2 \rangle, \quad k_T(t) = \tfrac{1}{2}\langle T'^2 \rangle \quad \text{and} \quad k_q(t) = \tfrac{1}{2}\langle q_v'^2 \rangle. \tag{3.1a–c}$$

The TKE profile is depicted in figure 3. We also display the mean of the kinetic energy dissipation rate field,

$$\langle \epsilon(t) \rangle = 2\nu \langle S_{ij} S_{ji} \rangle \quad \text{with} \quad S_{ij} = \frac{1}{2}\left(\frac{\partial u_i}{\partial x_j} + \frac{\partial u_j}{\partial x_i} \right), \tag{3.2}$$

as well as the means $\langle q_v(t) \rangle$ and $\langle T(t) \rangle$. The brackets $\langle \cdot \rangle$ denote again spatial averaging over the whole simulation domain $V = V_1 \cup V_2$ (see figure 2).

In order to obtain the balance equations for quantities (3.1*a–c*), we multiply the three momentum balance equations with the corresponding u_i, which implies automatically the Einstein's summation rule, the temperature fluctuation equation with T' and the one for the water vapour mixing ratio fluctuations with q_v', respectively. After taking the volume average, applying Gauss's theorem and using the fact that flux terms across the boundary disappear in the case of periodic sidewalls, we arrive

https://doi.org/10.1017/jfm.2017.23 Published online by Cambridge University Press

at the evolution equations, which are given by

$$\frac{\mathrm{d}k}{\mathrm{d}t} = \langle u_z B\rangle - \langle\epsilon\rangle, \tag{3.3}$$

$$\frac{\mathrm{d}k_q}{\mathrm{d}t} = -\langle\epsilon_q\rangle - \langle C_d' q_v'\rangle, \tag{3.4}$$

$$\frac{\mathrm{d}k_T}{\mathrm{d}t} = -\langle\epsilon_T\rangle + \frac{L}{c_p}\langle C_d' T'\rangle. \tag{3.5}$$

Quantities $\langle\epsilon_q(t)\rangle = D\langle|\nabla q_v'|^2\rangle$ and $\langle\epsilon_T(t)\rangle = \kappa\langle|\nabla T'|^2\rangle$ are the dissipation rate of vapour variance and the thermal dissipation rate, respectively. We will focus on describing the TKE balance (3.3) in the following because the other two quantities, k_q and k_T, decay steadily for most of the time during the mixing process.

The buoyancy feeds back to the flow in three different ways – namely via temperature, vapour and liquid water contents – and thus contributes to the TKE production via the buoyancy flux term in (3.3). Droplets that enter the subsaturated region will shrink and thus cause a local evaporative cooling. This will lower the magnitude of the adjacent temperature field and, together with the additional drag due to gravitational settling of the droplets, results in a negative local buoyancy contribution ($B < 0$). A downdraught eventually forms due to gravitational acceleration ($u_z < 0$) such that the product of the two quantities turns into a local gain term ($u_z B > 0$) for the TKE. A local loss will be caused by an updraught $u_z > 0$ and $B < 0$. The kinetic energy dissipation rate is a positive definite quantity and thus always a sink of TKE.

Following from figure 3 for the TKE, the mixing process can be divided into four different stages:

(i) The first stage lasts the first half eddy turnover time and is characterized by a very rapid decay of turbulence. The small eddies are dissipated quickly until the first droplets start to evaporate and consume heat in their vicinity. The end of this period is marked by a dotted line in figure 3(*a*,*b*).

(ii) The second stage displays a recovery of TKE due to the combined action of velocity downdraught and negative buoyancy. Consequently, kinetic energy dissipation also increases. Both k and $\langle\epsilon\rangle$ reach a local maximum after up to two eddy turnover times indicated by a second dotted line in figure 3(*a*,*b*). The large-scale eddy turnover time at the end of this period $T_{L,B}$ (see table 3) is chosen as the reference time for further comparison.

(iii) The third stage starts when production and dissipation of kinetic energy are of nearly the same size. The mixing process now passes through a phase that is close to statistical stationarity, at least in terms of the TKE. This period lasts approximately four eddy turnover times in configurations TNIa and TTIa. It is expected to take longer in the larger domain of run TNIb, but computational resources limited the time that could be followed for that case. Significant buoyancy production is achieved on the one hand when a large portion of cloudy air with droplets entrains the clear air region, which is the case during this stage of evolution. The time this takes is given by the large-eddy turnover time T_L. In order to cause colder downdraughts, on the other hand, droplets have to evaporate. This time interval is quantified by the phase relaxation time τ_{ph} and the single droplet evaporation time τ_{ev}, depending on their relative magnitudes (Lehmann *et al.* 2009). Definitions and typical values for these time scales are given in table 3. For this stage $\langle\epsilon\rangle \approx 10$ cm^2 s^{-3} in all cases, which results in $\eta_K \approx 1.35$ mm and $R_\lambda = 187$, 133 and 419 for TNIa, TTIa and TNIb, respectively.

https://doi.org/10.1017/jfm.2017.23 Published online by Cambridge University Press

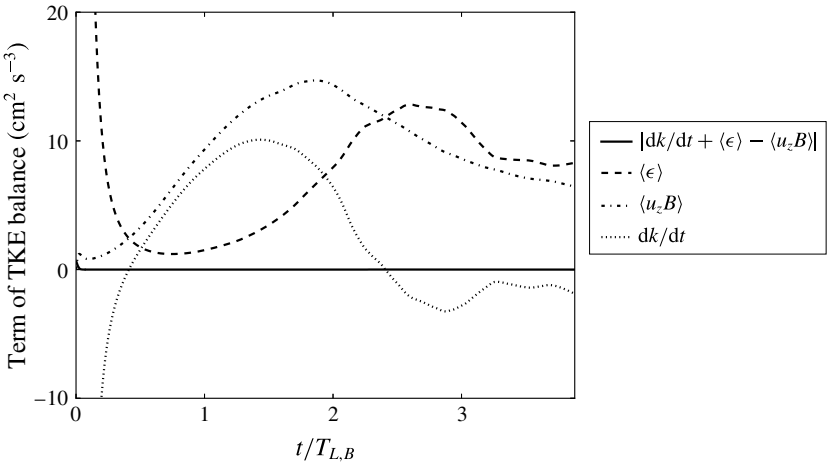


FIGURE 4. Time evolution of the three terms of the TKE balance (3.3). Data for case TNIa are displayed. The solid line stands for the difference of the left-hand side (l.h.s.) and right-hand side (r.h.s.) of the equation. The absolute error, |l.h.s. − r.h.s.|, remains below 10^{-3} for most of the integration time. Recall that accuracy is lost when point droplets are extrapolated to the nearest grid points in order to calculate q_l and C_d.

(iv) The fourth and final stage starts after approximately six eddy turnover times and marks the eventual decay of all quantities and the finalization of the mixing process in our system. The mean temperature approaches the estimate that we obtained from (2.19) and (2.20). This value of $T_\infty = 290.2$ K is indicated by a dashed line in figure 3(*d*). The total temperature variation remains small in the course of the evolution. As seen in figure 3(*d*), there is a total drop by $\Delta T = 2.5$ K. For these variations, we can keep all material parameters as constants (see also Zonta & Soldati (2014) for a study of temperature-dependent effects).

To all panels of figure 3, we add the data from the run in the largest domain, TNIb. A larger TKE for TNIb is in line with a larger domain and larger Reynolds number. Note also that the eddy turnover time, T_L, becomes larger compared to TNIa (see table 3).

In figure 4, we plot the different terms of the TKE balance separately for times up to four eddy turnover times for run TNIa. The rapid initial temporal variation of the TKE is mostly due to dissipation. The latter decreases rapidly while the buoyancy production term gains magnitude. Clearly visible is also how both terms on the right-hand side of (3.3) reach approximately the same magnitude and compensate each other. This causes the nearly statistically stationary regime for times $t \gtrsim 2T_{L,B}$. Although not shown, we found that k_q decays monotonically throughout the mixing process, while k_T increases together with the initial recovery of k but decays afterwards. Evaporative cooling produces local cold patches that enhance the temperature fluctuations. In general, fluctuations for both scalars decay rapidly. For both fields the decay proceeds more slowly for the shearless mixing case TNI in comparison to case TTI because the transport across the interface proceeds more slowly. We will come back to this point in § 3.2.

https://doi.org/10.1017/jfm.2017.23 Published online by Cambridge University Press

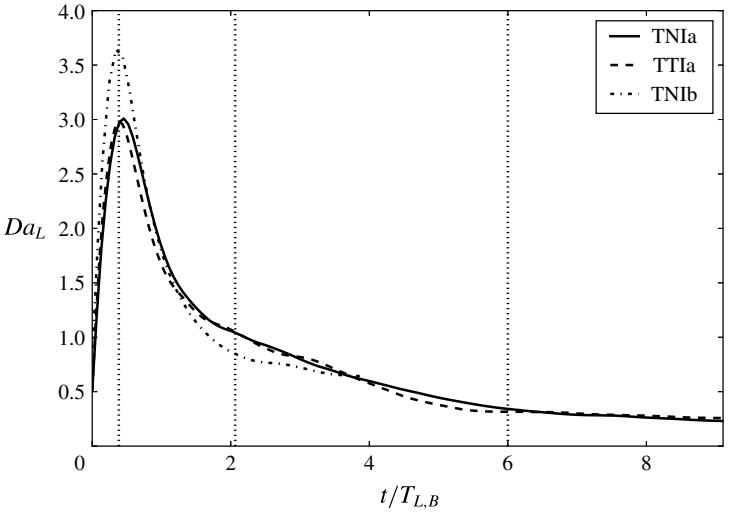


FIGURE 5. Large-scale Damköhler number $Da_L(t)$ as defined in (3.6) for the three runs. The four stages of the evolution are indicated again by vertical dotted lines (see also table 3).

3.2. *Damköhler number versus time*

As we have stated at the beginning of § 3.1, the mixing process is transient over the whole period, which implies that the turbulence time scales keep changing. Therefore, in table 3 we have listed times that are either based on initial conditions or taken at time instants indicated in figure 3. In order to get a better idea about the transient character of the mixing process, we show in figure 5 the Damköhler number as a function of time for the three different runs. The Damköhler number relates a fluid time scale to a reaction (or evaporation) time scale. Based on the large-eddy turnover time, it is given by

$$Da_L(t) = \frac{T_L(t)}{\tau_{ph}(t)} = \frac{4\pi D' L_x \langle n_d(t)\rangle_{V_1} \langle r(t)\rangle_{V_1}}{\sqrt{\langle u_i^2(t)\rangle_{V_1}}}. \tag{3.6}$$

Equation (3.6) is based on the cloudy half of the slab, V_1. We observe in figure 5 that the values of $Da_L(t)$ exceed unity by almost a factor of 4 in magnitude in the initial stage of the evolution. The bigger the simulation domain, the larger the local maximum in $Da_L(t)$. This means that the dynamical process leads to a transient inhomogeneous mixing regime (Lehmann *et al.* 2009). Our results suggest that this regime becomes increasingly important as the size of the computational domain grows. Figure 6 shows a vertical cut in TNIb for two instants. The inhomogeneous mixing becomes visible. Domains inside the cloud that are still unaffected by the entrainment coexist with domains that are already strongly mixed.

3.3. *Time evolution of plane-averaged profiles across the mixing layer*

In order to understand the temporal behaviour of the TKE and the other quantities better, we refine our analysis by averaging over the two statistically homogeneous space directions and studying the profiles along the inhomogeneous x direction.

https://doi.org/10.1017/jfm.2017.23 Published online by Cambridge University Press

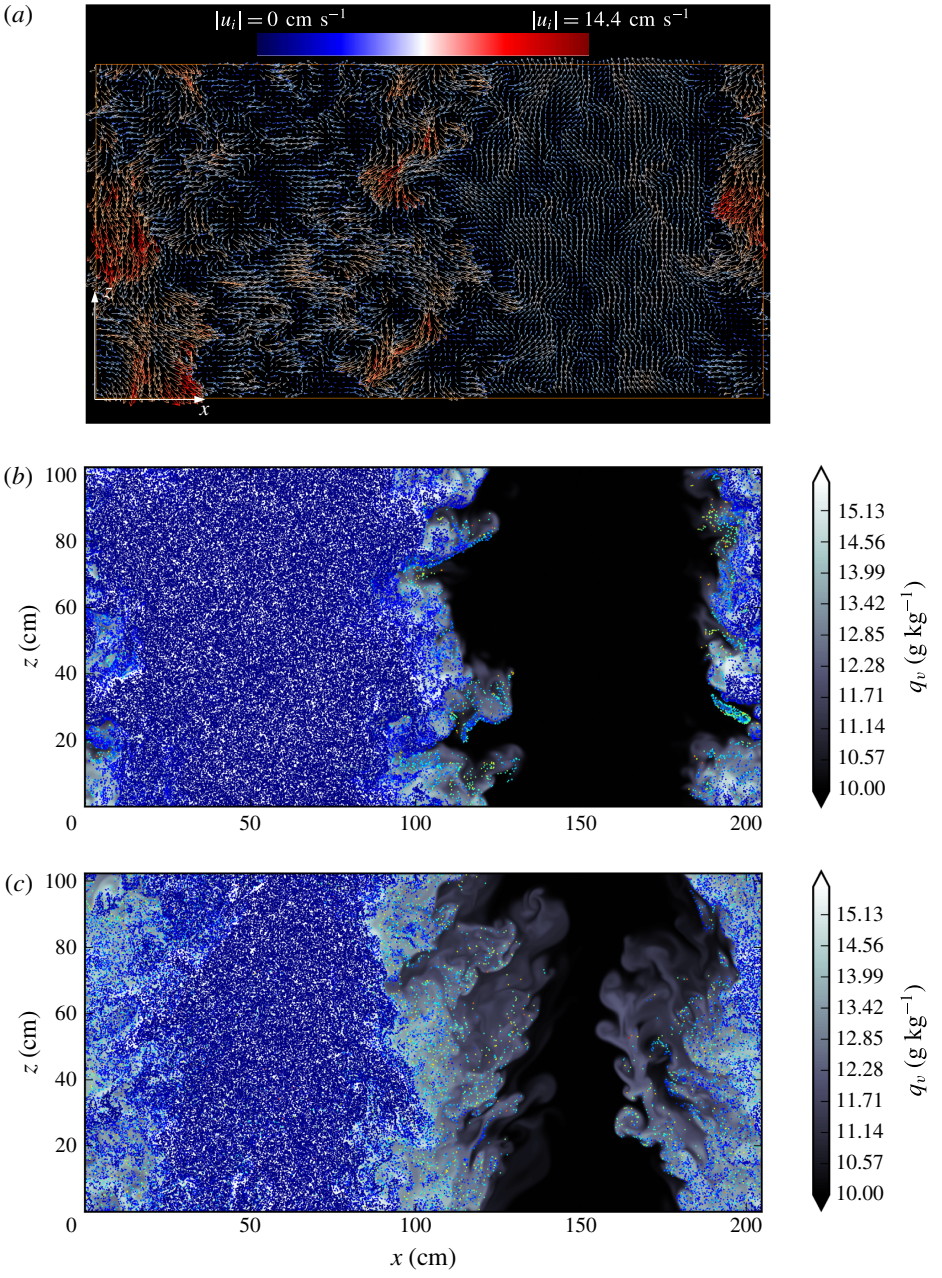


FIGURE 6. Snapshots of the velocity field at $t \approx 4$ s or $0.4\,T_{L,B}$ (*a*) and the vapour mixing ratio field q_v together with the droplet distribution (*b*,*c*). All data are taken in the midplane $y = L_y/2$. Panel (*b*) is also taken at $t \approx 4$ s and panel (*c*) at $t \approx 16$ s or $1.6\,T_{L,B}$. Data are for TNIb. The colour legend is given for q_v. Individual cloud droplets are coloured with respect to their radius. Deep blue stands for $r = R_0 = 16$ μm and red for $r = 12$ μm. The downdraughts are mostly correlated with the largest velocity magnitudes in panel (*a*).

https://doi.org/10.1017/jfm.2017.23 Published online by Cambridge University Press

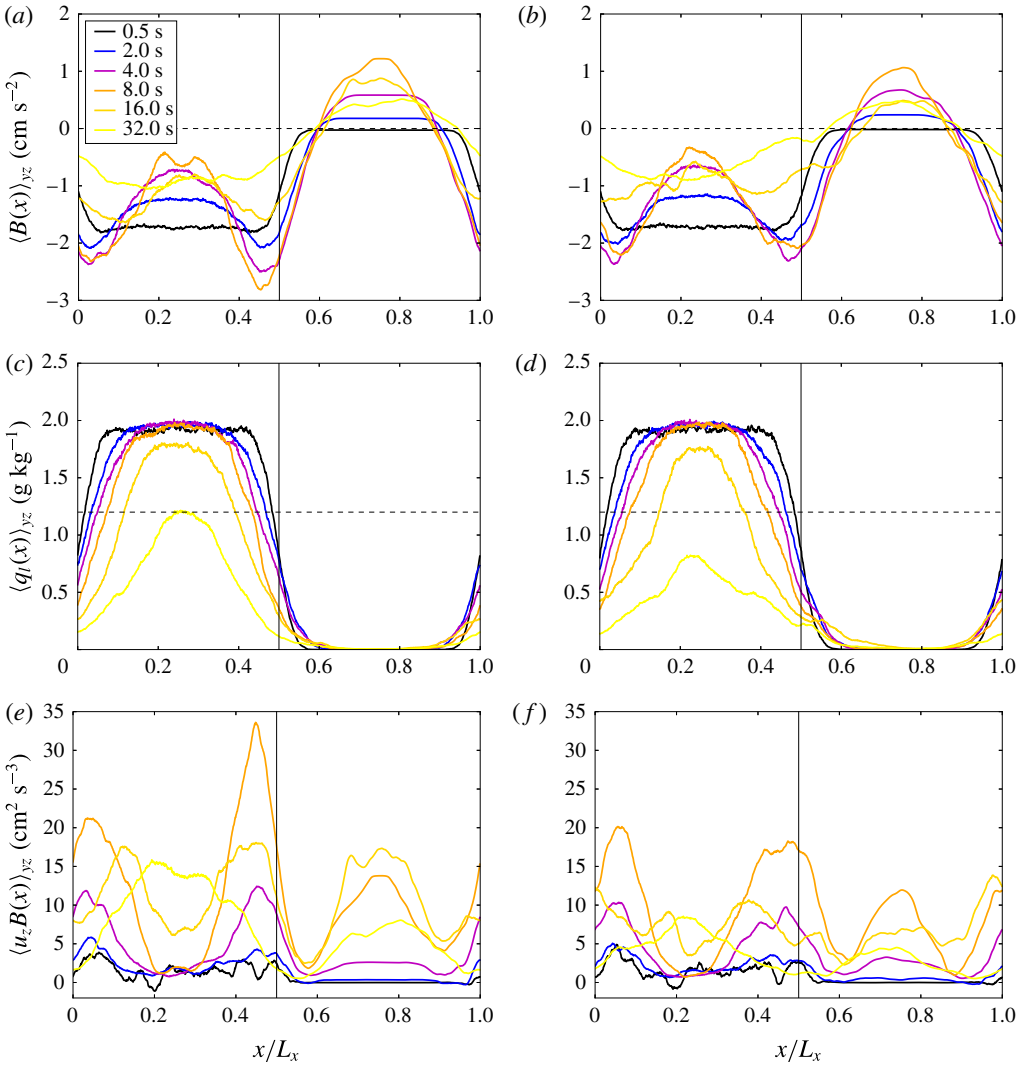


FIGURE 7. (Colour online) Evolution of plane-averaged profiles of (*a*,*b*) buoyancy $\langle B(x)\rangle_{yz}$, (*c*,*d*) liquid water content $\langle q_l(x)\rangle_{yz}$ and (*e*,*f*) production of TKE $\langle u_z B(x)\rangle_{yz}$ due to buoyancy. (*a*,*c*,*e*) For case TNIa, and (*b*,*d*,*f*) for case TTIa as summarized in table 1. The dashed lines in the plots are added as a guide to the eye.

Therefore we average with respect to the vertical y–z planes, i.e. planes that are parallel to the interface. The profiles are denoted by $\langle\cdot(x)\rangle_{yz}$. Figure 7 shows profiles of buoyancy B (*a*,*b*), liquid water mixing ratio q_l (*c*,*d*) and convective buoyancy flux (*e*,*f*) at different times as indicated in the legend.

Our simulation resembles the situation of a dissolving cloud with negative buoyancy in the cloud core, which is established here solely by the initially added droplets. The cases TNIa (*a*,*c*,*e*) and TTIa (*b*,*d*,*f*) are compared. At the initial stage the cloud slab contains all the droplets and those that are near the interface start to evaporate slowly. Therefore, negative buoyancy is enhanced at the cloud–clear air interface, visible as new local minima in the buoyancy profile. These minima

https://doi.org/10.1017/jfm.2017.23 Published online by Cambridge University Press

are more pronounced for TNIa. Here, cloud droplets enter an environment with a significantly lower TKE and are decelerated compared to TTIa. For the latter they are advected further due to the same amplitude of velocity fluctuations in- and outside the cloud. The TKE contrast in case TNIa accelerates the decoupling of droplets due to gravitational settling and thus results in larger contributions to $B = -gq_l$ (see (2.5)). This causes the slightly larger magnitudes of $\langle B(x)\rangle_{yz}$ when TNIa is compared to TTIa in figure 7(*a*,*b*).

The profiles confirm also that the TTI set-up enhances entrainment for times larger than $T_{L,B}$ (see also table 3). This can be clearly seen in the liquid water profiles $\langle q_l(x)\rangle_{yz}$, e.g. by a comparison at $t = 32$ s or $4\,T_{L,B}$. In the TTIa case, the liquid water content is significantly reduced compared with TNIa at the same time t. The stronger buoyancy minimum at the interface and the reduced lateral transport are responsible for a stronger TKE production due to the convective buoyancy flux $\langle u_z B(x)\rangle_{yz}$, as seen in figure 7(*e*,*f*). The role of evaporative cooling for the generation of TKE has been stressed by Malinowski *et al.* (2008) and Mellado (2010), and we see that this indeed is a dominant factor in the evolution, especially for the shearless mixing layer TNIa.

3.4. *Growth of the mixing layer*

Since the cloud–clear air interface is not resolved in most large-eddy simulations of turbulent clouds, the growth of the mixing layer has to be modelled. In this subsection, we determine this growth of the mixing layer from our simulation data. This provides a measure for the entrainment velocity. We will use here the kurtosis of the vapour mixing ratio field to quantify the growth. This positive definite quantity is exactly one in the unmixed regions inside and outside the cloud and larger than one in regions where the mixing and entrainment proceeds. Other measures based on vorticity are possible as discussed for example in the review by da Silva *et al.* (2014). Specifically, we calculate

$$K(q_v) = \frac{\langle q_v^4(x)\rangle_{yz}}{\langle q_v^2(x)\rangle_{yz}^2}, \tag{3.7}$$

and show the resulting profiles in figure 8(*a*,*c*). Again, cases TNIa and TTIa are compared. The width of the mixing layer is taken as the width of the profile at half the maximum. It is denoted by $\Delta(t)$ and shown in figure 8(*b*). The width remains comparable during the first stage of the mixing process. With the beginning of the second phase for times $t \gtrsim 0.5T_{L,B}$, we observe that the width of the layer grows faster for TTI, which is consistent with the more rapid increase of the mean vapour content in § 3.1. One may conclude, therefore, that the early progression of the mixing process is dominated by the eddy structure in the cloudy region, with relatively small differences between TNIa and TTIa, but at larger times the evolution diverges due primarily to the differing TKE levels.

3.5. *Enstrophy and shear production in the mixing layer*

As we showed in § 3.3, the negative buoyancy due to evaporative cooling generates kinetic energy. A shear layer is formed in the interface region, which generates a dominantly upward motion outside the cloud and downward motion inside the cloud. These shear layers are a main source for enhanced turbulent fluctuations and thus for kinetic energy dissipation. In order to study this aspect in more detail, we display in figure 9 isosurfaces of the local enstrophy and the kinetic energy dissipation fields. The vorticity is given by

$$\omega_i(x_m, t) = \epsilon_{ijk}\frac{\partial u_k}{\partial x_j}, \tag{3.8}$$

https://doi.org/10.1017/jfm.2017.23 Published online by Cambridge University Press

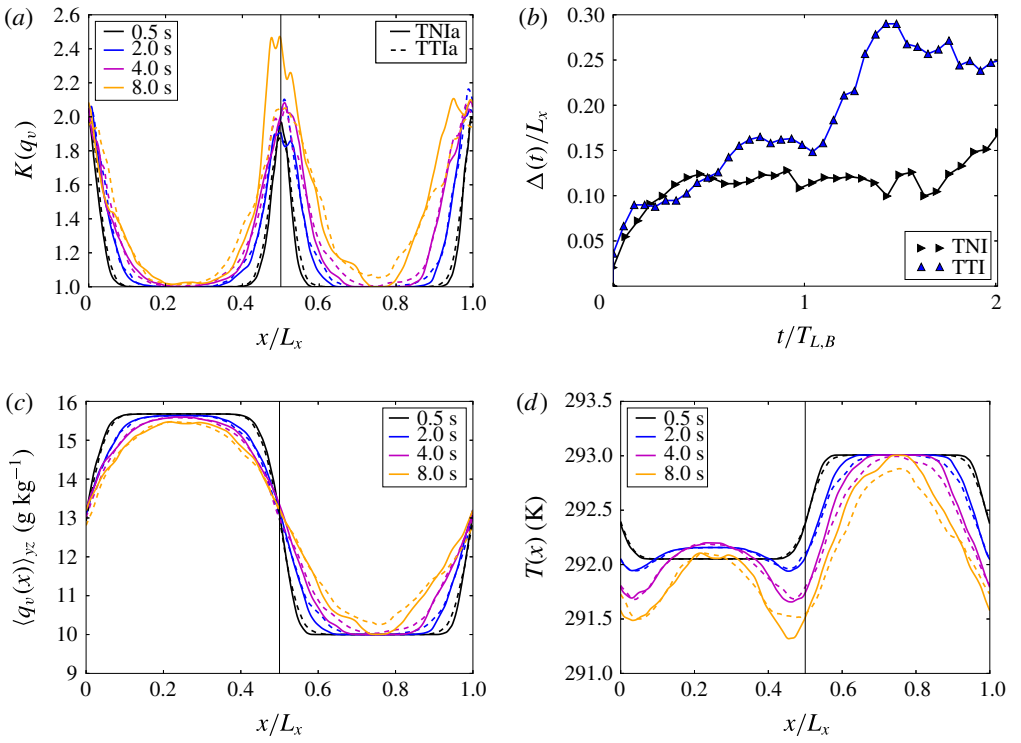


FIGURE 8. (Colour online) Growth of the mixing layer with respect to time. (*a*) Evolution of the kurtosis $K(q_v)$ as a function of time. (*b*) Growth of the width of the mixing layer, $\Delta(t)$, with respect to time. Again the two cases TNIa and TTIa are compared. The time axis is rescaled by the corresponding large-eddy turnover time $T_{L,B}$, which is 7.7 s in case TNIa and 9.1 s for TTIa. For comparison we show the profiles of plane-averaged vapour mixing ratio (*c*) and temperature (*d*).

with ϵ_{ijk} being the Levi-Civita symbol. The local enstrophy is the squared magnitude of the vorticity, $\omega^2 = \omega_i\omega_i$. The kinetic energy dissipation rate field is defined in (3.2). We recall that the two ensemble averages are connected in homogeneous isotropic turbulence by

$$\langle\epsilon\rangle = \nu\langle\omega^2\rangle. \tag{3.9}$$

Isolevels of both fields are shown at a fixed value for all three time instants. The snapshots are taken at times $t \approx 4$ s, $t \approx 16$ s and $t \approx 32$ s (or approximately 0.4, 1.6 and 3.1 $T_{L,B}$) for the biggest shearless mixing layer run, TNIb. Initially, fine-scale structures of both quantities are visible primarily in the left part of the box in which the TKE has a larger amplitude. As the turbulence decays, smaller eddies are dissipated, leading to coarser structures. Owing to evaporative cooling, up- and downdraughts are generated, producing the largest shear and vorticity events at the interface, as is visible in figure 9(*b*). In figure 9(*c*) it is clearly visible that, in the later stage of the evolution, the high-amplitude events are now located in- and outside the original cloud location. At time $t = 32$ s the droplets have spread into the clear air region, and have evaporated and generated smaller flow structures due to evaporative cooling and gravitational settling. This now generates most of the dissipation and local enstrophy. Figure 9 shows that the isocontours of energy dissipation and local

https://doi.org/10.1017/jfm.2017.23 Published online by Cambridge University Press

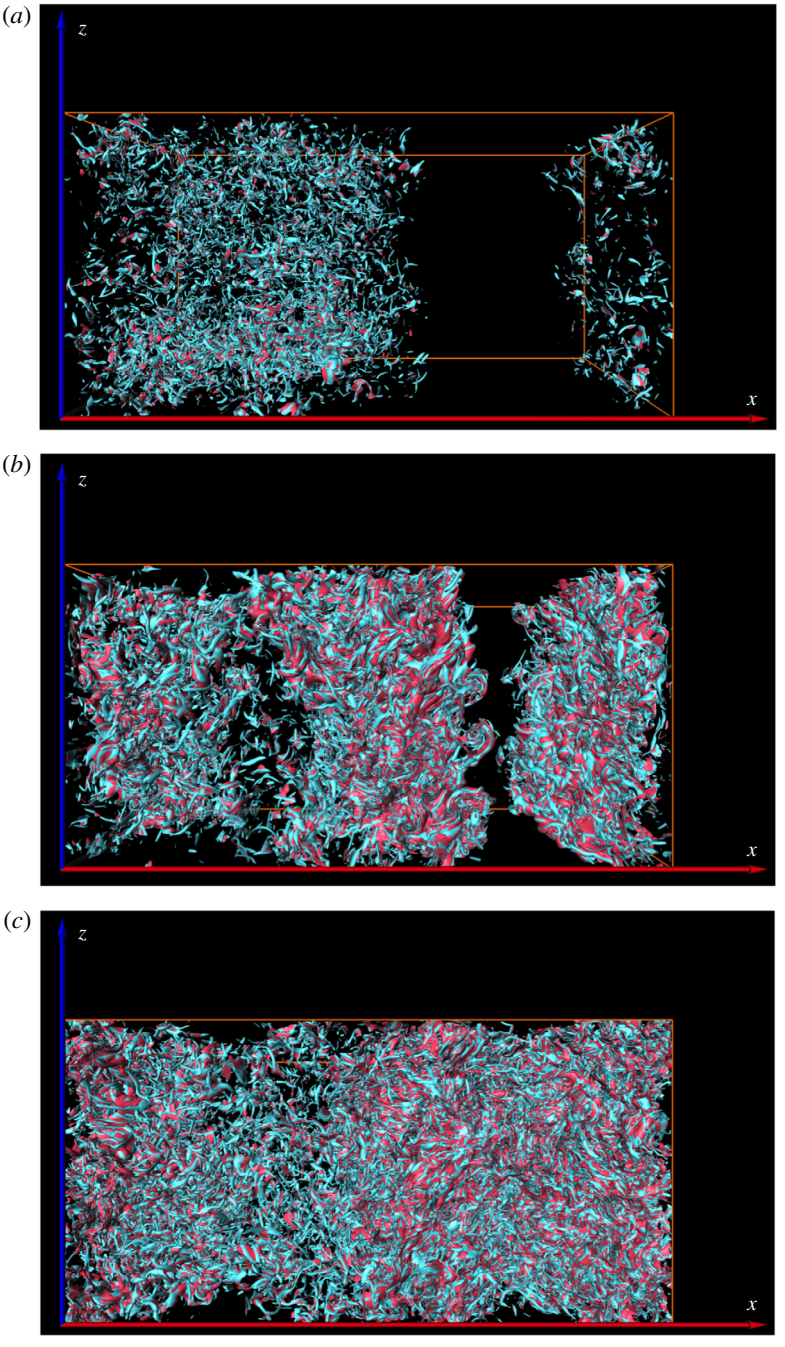


FIGURE 9. Isosurfaces of the local enstrophy (blue) and kinetic energy dissipation (red) for different times. Times are $t \approx 4$ s (*a*), $t \approx 16$ s (*b*) and $t \approx 32$ s (*c*). The view is on the front face of the domain. Initially, the cloudy fraction occupies the left half of the box. Data are for run TNIb. The isolevels for the three panels are $\epsilon = 32$ cm^2 s^{-3} and $\omega^2 = 213$ s^{-2} such that $\epsilon = \nu\omega^2$. Times correspond to 0.4, 1.6 and 3.1 eddy turnover times $T_{L,B}$.

https://doi.org/10.1017/jfm.2017.23 Published online by Cambridge University Press

enstrophy are always found together, a result which is known from other flows such as homogeneous isotropic turbulence (Schumacher, Eckhardt & Doering 2010). The levels of both isocontours have been chosen such that $\epsilon = \nu\omega^2$. The exact relation (3.9) for the mean values of both fields is also locally quite well established.

The production of shear and vorticity can be discussed by means of the balance equations for shear magnitude and local enstrophy. The vorticity equation follows from (2.2) as

$$\frac{\partial \omega_i}{\partial t} + u_j \frac{\partial \omega_i}{\partial x_j} = \omega_j \frac{\partial u_i}{\partial x_j} + \nu \frac{\partial^2 \omega_i}{\partial x_j^2} + \epsilon_{zik} \frac{\partial B}{\partial x_k}, \tag{3.10}$$

with an additional term due to buoyancy on the right-hand side. It results in a balance for the local enstrophy of

$$\frac{\mathrm{d}\omega^2}{\mathrm{d}t} = \underbrace{2\omega_i S_{ij} \omega_j}_{=P_{\omega S}} + 2\nu\omega_i \frac{\partial^2 \omega_i}{\partial x_j^2} + \underbrace{2\epsilon_{zik}\omega_i \frac{\partial B}{\partial x_k}}_{=P_{\omega B}}. \tag{3.11}$$

The evolution of the ij component of the rate-of-strain tensor is given by

$$\frac{\partial S_{ij}}{\partial t} + u_k \frac{\partial S_{ij}}{\partial x_k} = -S_{ik}S_{kj} - \frac{1}{4}(\omega_i\omega_j - \delta_{ij}\omega_k^2) - \frac{1}{\rho_0}P_{ij} + \nu \frac{\partial^2 S_{ij}}{\partial x_k^2} + \frac{1}{2}\left(\delta_{zi}\frac{\partial B}{\partial x_j} + \delta_{zj}\frac{\partial B}{\partial x_i}\right). \tag{3.12}$$

A similar balance as for the local enstrophy follows for the magnitude square of the strain $S^2 = S_{ij}S_{ji}$, given by

$$\frac{\mathrm{d}S^2}{\mathrm{d}t} = \underbrace{-(2S_{ij}S_{jk}S_{ki} + \frac{1}{2}\omega_i S_{ij}\omega_j)}_{=P_S} - 2S_{ij}\frac{1}{\rho_0}P_{ij} + 2\nu S_{ij}\frac{\partial^2 S_{ij}}{\partial x_k^2} + \underbrace{2S_{zi}\frac{\partial B}{\partial x_i}}_{=P_{SB}}, \tag{3.13}$$

where the pressure Hessian P_{ij} is defined as

$$P_{ij} = \frac{\partial^2 p}{\partial x_i \partial x_j}. \tag{3.14}$$

Equation (3.11) contains the enstrophy production term $P_{\omega S} = 2\omega_i S_{ij}\omega_j$ due to vortex stretching. This term enters also the strain production balance in (3.13), which is given by $P_S = -2S_{ij}S_{jk}S_{ki} - \omega_i S_{ij}\omega_j/2$. Both equations contain production terms due to the buoyancy feedback, $P_{\omega B} = 2\epsilon_{zik}\omega_i\partial_k B$ in (3.11) and $P_{SB} = 2S_{zi}\partial_i B$ in (3.13). The non-local pressure–strain coupling is not investigated more closely here as well as the dissipative terms in both balance equations.

In figures 10 and 11 we analyse the different production terms that appear in (3.11) and (3.13). Averages over y–z planes versus the x coordinate perpendicular to the initial cloud–clear air interface are shown again. Figure 10 is taken at $t = 16$ s and figure 11 at $t = 32$ s. Panels (a,c) in figures 10 and 11 display the production terms, $P_{\omega S}$ and P_S, and panels (b,d) show enstrophy and strain production due to the coupling between buoyancy and the vertical velocity component, $P_{\omega B}$ and P_{SB}. In Schumacher, Götzfried & Scheel (2015) it was shown that $P_{\omega B} \ll P_{\omega S}$ for standard Rayleigh–Bénard convection. This result can be confirmed here and even extended to the strain balance. Furthermore, it can be seen that there are significant differences between cases TNIa and TTIa. They become larger as the time proceeds and are

https://doi.org/10.1017/jfm.2017.23 Published online by Cambridge University Press

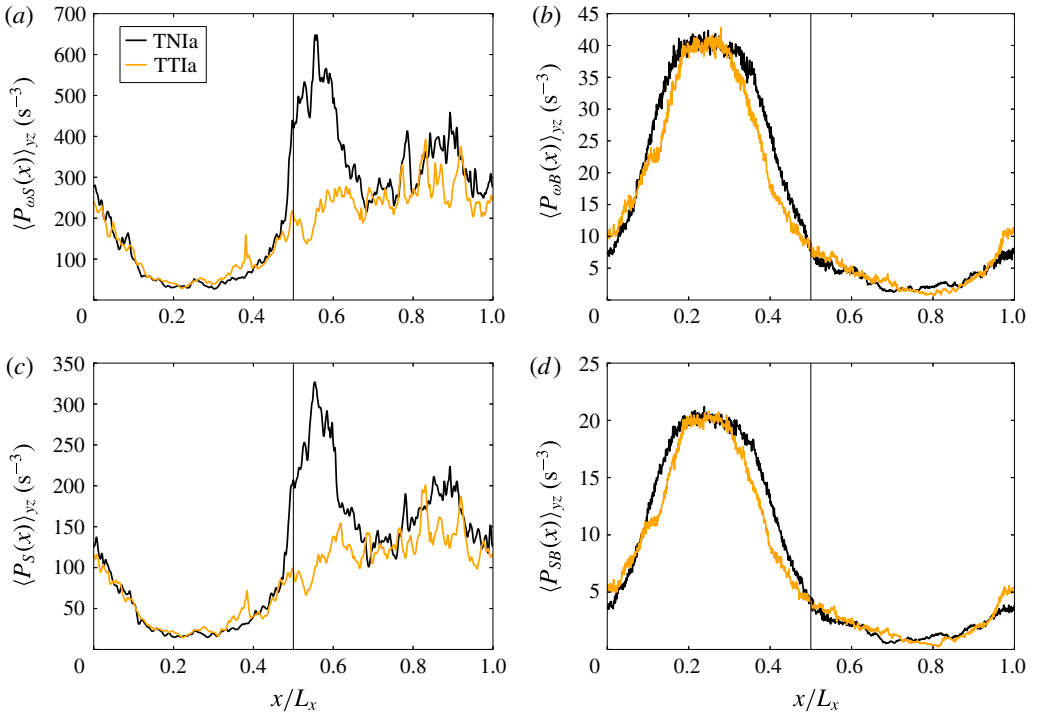


FIGURE 10. (Colour online) Production of enstrophy and strain in the mixing layer. Similar to figure 7, we display profiles that are obtained by averages over y–z planes at time $t = 16$ s. (*a*) Enstrophy production due to vortex stretching, $P_{\omega S}$. (*b*) Enstrophy production due to buoyancy, $P_{\omega B}$. (*c*) Strain production due to strain–strain coupling. (*d*) Strain production due to buoyancy, P_{SB}.

strongest for $P_{\omega S}$ and P_S, respectively. For $t = 16$ s, the strong peak of $P_{\omega S}$ and P_S at the interface is absent in the case of TTIa, in which no gradient of turbulence intensity exists. A $t = 32$ s, case TTIa obeys an almost homogeneous production profile for $P_{\omega S}$ and P_S. Furthermore, both buoyancy production terms are significantly smaller in amplitude.

The profiles of $P_{\omega S}$ and P_S are almost identical and differ in magnitude only. The same holds for $P_{\omega B}$ when compared with P_{SB}. Both reflect the tight interplay between strain and enstrophy generation. Furthermore, figures 10 and 11 show that the small-scale turbulence is strongly altered when the turbulence levels inside and outside the cloud differ, a result that was much less clearly visible from macroscopic quantities that we have compared in the preceding sections. Our studies show that the local strain and enstrophy production are mostly caused by the nonlinear coupling of the fluid turbulence, which however has its origin in the buoyancy feedback.

4. Response of droplet ensemble to the mixing process

4.1. *Droplet trajectories at the interface*

In figure 6 we saw that a subset of the droplets remains for a long time inside the cloud core while other subsets at the cloud edge have already been completely evaporated. This is the central idea of an inhomogeneous mixing scenario.

https://doi.org/10.1017/jfm.2017.23 Published online by Cambridge University Press

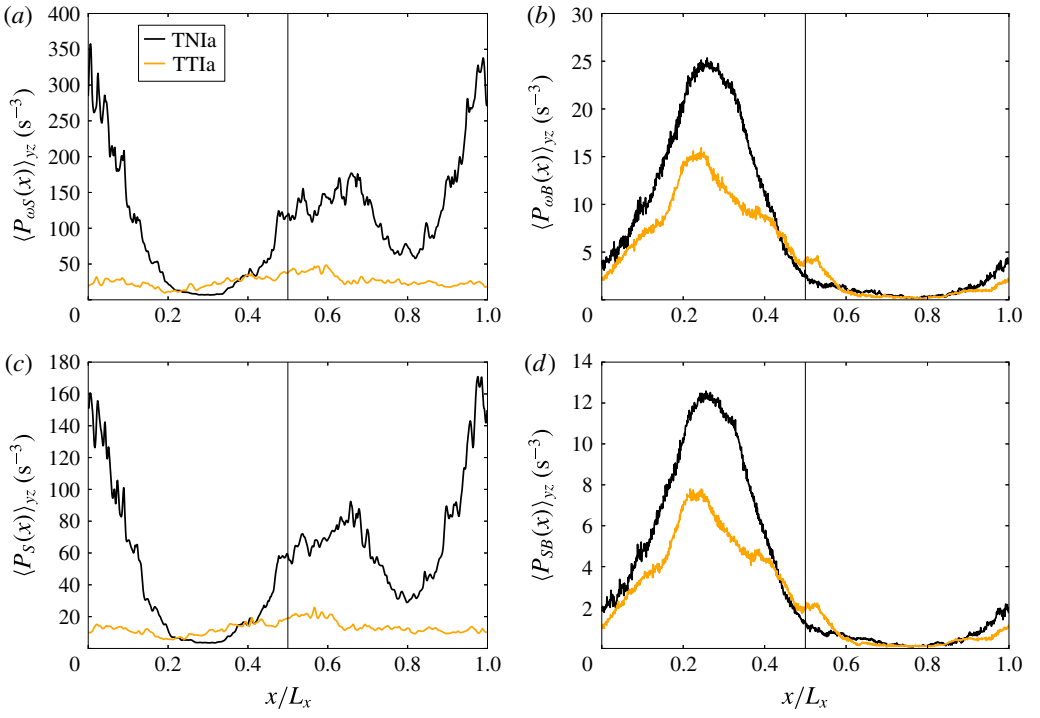


FIGURE 11. (Colour online) Same data as in figure 10 for $t = 32$ s.

In the following we extract such subsets of particles and examine the thermodynamic properties along their trajectories. Therefore, we divide the droplets into three categories: droplets that evaporate very quickly by entering the subsaturated cloud environment immediately; droplets that enter the subsaturated area and return back into the cloud filament; and droplets that remain inside the cloud core for a long time. In order to track any given particle location and its thermodynamic properties, we saved the quantities with a time resolution of $\Delta t = 0.05$ s. Typical particle trajectories and thermodynamic properties such as temperature T, supersaturation S and vertical droplet velocity component V_z are displayed in figure 12 for TNIa. The trajectories are plotted until a time $t = 5$ s, which corresponds to $0.65\,T_{L,B}$.

The most interesting case is shown in figure 12(*b*,*e*,*h*,*k*), where particles enter the subsaturated region and then return back into the cloudy region. On their way they experience temperatures below the initial cloud temperature of $T_c = 292.0$ K. Being initially in a strongly subsaturated state, they return back to a more humid environment that is still subsaturated. This is sufficient for the droplets to fully evaporate although they again enter the cloud interface. Droplets inside the cloud core as shown by figure 12(*c*,*f*,*i*,*l*) are moving downwards with negative vertical velocity due to the overall drag included in the buoyancy, as given by (2.5). Initially they are in a supersaturated state and can grow in radius by condensation. This is visible by a slight temperature increase since latent heat is released. The supersaturation decays slowly exponentially to values close to zero. This subset represents the majority of cloud droplets, where the initial profile of the rescaling function was constant. Some droplets at the cloud edge enter the subsaturated area immediately as shown in figure 12(*a*,*d*,*g*,*j*). Initially, a jump in all thermodynamic values is visible

https://doi.org/10.1017/jfm.2017.23 Published online by Cambridge University Press

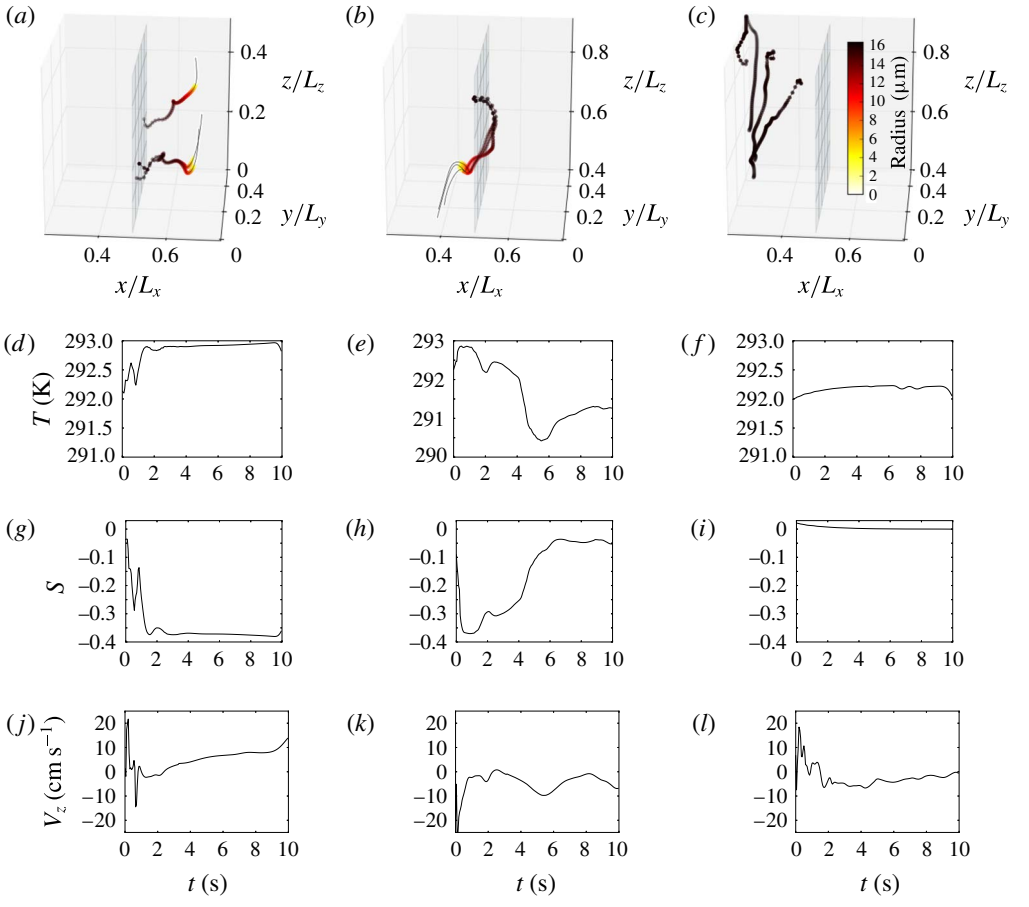


FIGURE 12. (Colour online) Droplet trajectories and plots of the corresponding temperature T, supersaturation S and vertical velocity V_z along the droplet paths for the cases where droplets evaporate fast (*a*,*d*,*g*,*j*), return back to the initial cloud domain (*b*,*e*,*h*,*k*) or stay inside the cloud (*c*,*f*,*i*,*l*). The plane in the trajectory plots marks the initial interface between cloudy and clear air subdomains. Data are obtained from TNIa. Thin solid lines in trajectory plots indicate droplets that are practically evaporated.

where droplets change from positive vertical velocity suddenly to negative values. This sudden changes occur as particles pass the interface. Once they are evaporated and far away from the interface, they experience a positive updraught.

4.2. *Distribution of droplet size and supersaturation*

Cloud droplet radius evolves in time as mixing progresses and, until complete evaporation occurs, the supersaturation and the temperature at the droplet positions will also vary in time. Prior Lagrangian simulations of mixing at the edge of a cloud by Kumar *et al.* (2012, 2014) and Perrin & Jonker (2015) showed that entrainment of subsaturated air leads to a broadening of the particle size distribution with extended exponential tails to smaller radii. The growth of the droplet radii and thus the broadening of the tail on the right side of the droplet size distribution can proceed only for an initial period deep inside the cloud where supersaturation is positive. It

https://doi.org/10.1017/jfm.2017.23 Published online by Cambridge University Press

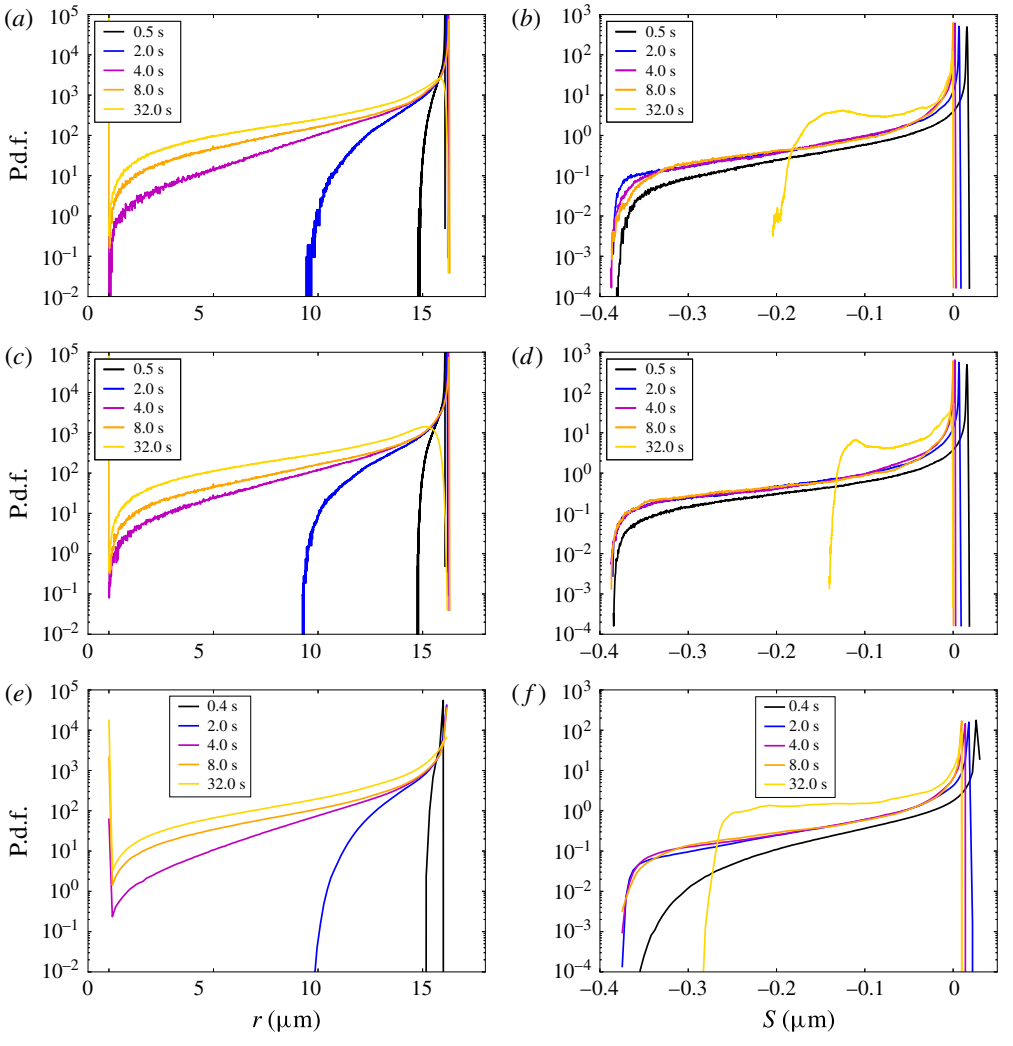


FIGURE 13. (Colour online) (*a*,*c*,*e*) Probability density functions (p.d.f.s) of cloud water droplet radius at different times are plotted for TNIa (*a*), TTIa (*c*) and TNIb (*e*). (*b*,*d*,*f*) The p.d.f.s of supersaturation at the same time instants, again for TNIa (*b*), TTIa (*d*) and TNIb (*f*).

remains a small effect in our study. In order to focus on the microphysical response to mixing, we do not include a supersaturation forcing term (Lanotte *et al.* 2009) and collisions and coalescence (Perrin & Jonker 2015).

Figure 13(*a*,*c*,*e*) shows the probability density function (p.d.f.) of the droplet radius for simulations TNIa (*a*), TTIa (*c*) and TNIb (*e*). Data are taken for the whole simulation domain. The comparison between TNIa and TTIa shows that slight differences occur in the evolution of the small droplet tail, with faster development occurring in the fully turbulent domain (TTIa). The comparison with TNIb shows that an increased size of the simulation domain and therefore of the Reynolds number leads to a somewhat slower growth of the left tail of the droplet size distribution. This is a result of the large-eddy turnover time for TNIb being greater than that

https://doi.org/10.1017/jfm.2017.23 Published online by Cambridge University Press

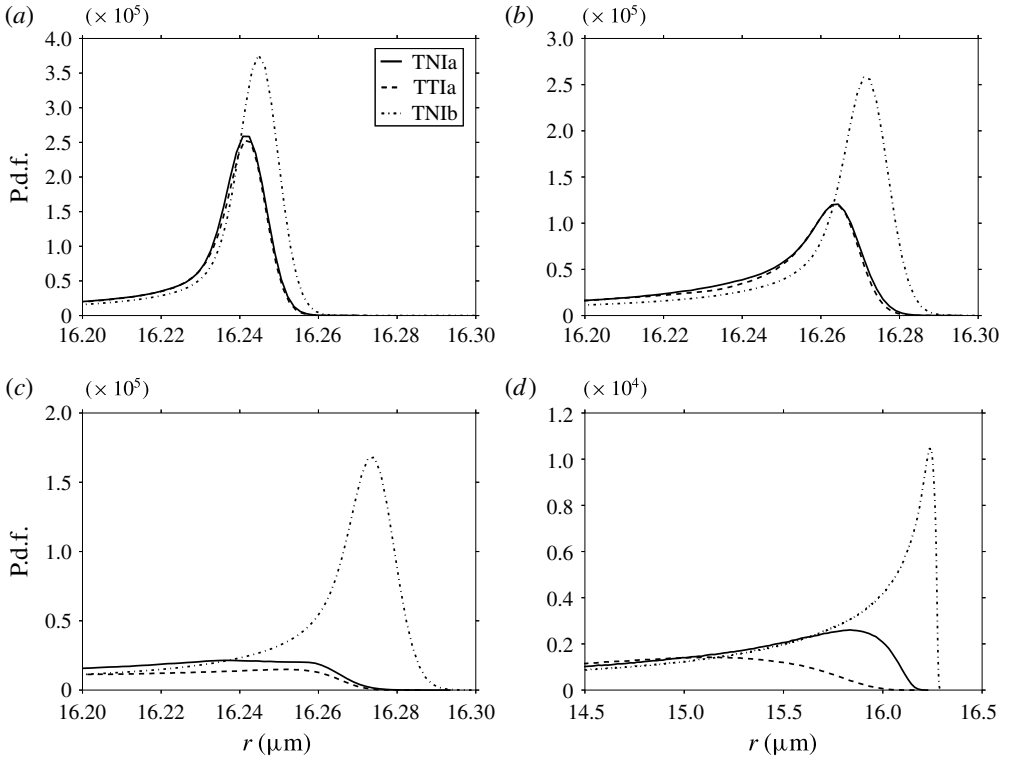


FIGURE 14. Zoomed view of the maximum of the droplet size distribution for the three runs at different times: (*a*) $t = 4$ s; (*b*) $t = 8$ s; (*c*) $t = 16$ s; (*d*) $t = 32$ s. The line styles for the different curves are indicated in the legend.

for TNIa. The differences in the size distributions are more evident in the zoomed plots shown in figure 14, in which we resolve, for different times, the peak of the distributions and the right tail where the largest droplets are observed. Here we clearly see that the differences between TNIa and TTIa are indeed small except for the last time. Presumably this is a result of the differing turbulence intensities in the two cases for times large compared to their corresponding eddy turnover time. The change in microphysical response as the computational domain size is increased (TNIa versus TNIb) is especially evident in this zoomed plot. The droplet size distribution remains much narrower in the larger domain, which is closer to the limit of extreme inhomogeneous mixing, i.e. the radius of most of the droplets remains unchanged for a longer time period during the mixing process. Figure 13(*b*,*d*,*f*) shows the p.d.f.s of supersaturation at the droplet locations (2.12) for the same simulation runs and the same times. They confirm that the majority of droplets remain close to the nearly saturated state ($S = 0$), with an exponential tail of subsaturated conditions. As with the droplet radius, slight differences in the left tails can be seen for TNIa and TTIa, especially at long times when the turbulence intensities are different. The same can be seen when TNIb is compared with TNIa. Here the reason is the larger domain, which leaves larger fractions of the cloud cores unmixed in the early stage, and in which mixing progresses more slowly due to the increase in large-eddy turnover time (see also figure 6).

https://doi.org/10.1017/jfm.2017.23 Published online by Cambridge University Press

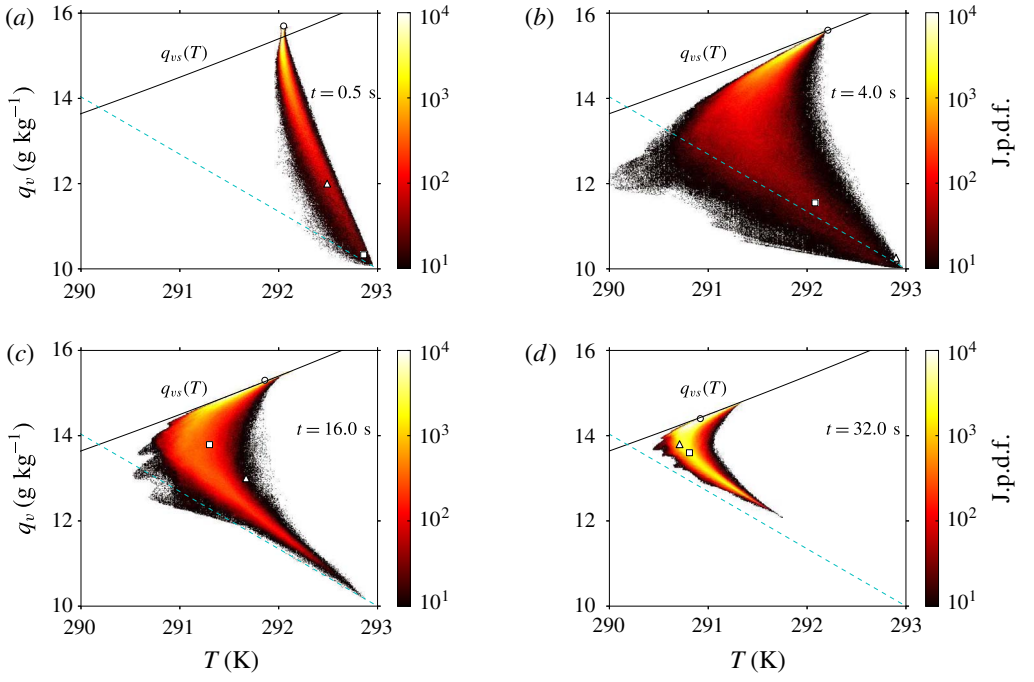


FIGURE 15. (Colour online) Time evolution of joint p.d.f. distribution for temperature T and water vapour mixing ratio q_v at the droplet positions, shown only for case TNIa. The solid line displays the dependence of the saturation vapour mixing ratio on temperature. The dashed line connects the initial state of the warmer cloud environment ($q_{ve}(t = 0)$, $T_e(t = 0)$ in the lower right with the point ($q_{vs}(T_\infty)$, T_∞). The triangles, squares and circles in the plots represent the thermodynamic state of three representative droplets, which evaporate very quickly outside the cloud, re-enter the cloudy domain and remain in the cloud core, respectively. Times correspond to approximately 0.07, 0.5, 2 and 4 eddy turnover times $T_{L,B}$.

4.3. *Droplet ensemble in temperature–vapour parameter plane*

The Lagrangian evolution of the droplet ensemble will now be displayed in a parameter plane that is spanned by vapour content and temperature. In this way, we provide a complementary view of the evolution of mixing that has been discussed in § 3.3 on the basis of plane-averaged profiles. We will also provide a connection to the three individual trajectories that have been examined in detail in § 4.1.

Figure 15 shows the joint probability density function (j.p.d.f.) of vapour mixing ratio q_v and temperature T taken at the particle positions for the TNIa case only; we saw that the TTIa case showed quite similar results. As already stated, the existence of a large latent heat leads to a decrease in the temperature T locally during droplet evaporation. The temperature decrease and the increase of water vapour content that occur during mixing and droplet evaporation are important to consider in detail because they both feed back to the flow via buoyancy, leading to vertical acceleration of the fluid. The solid line drawn in all the panels of figure 15 represents the saturation vapour mixing ratio, $q_{vs}(T)$, which is given by (2.13). Except for the early stage (see figure 15*a* for $t = 0.5$ s), the saturation threshold is not exceeded by the majority of the droplets. As the time proceeds, the distribution as a whole converges

https://doi.org/10.1017/jfm.2017.23 Published online by Cambridge University Press

to the $q_{vs}(T)$ line while spreading to lower temperatures. This line therefore marks the upper bound approached by all droplets as the mixing progresses. The dashed line in all the panels of figure 15 connects the initial state of the warmer clear air environment with $q_{ve}(t=0)=0.01$ and $T_e(t=0)=293$ K in the lower right, with the end point of the mixing process, $(q_{vs}(T_\infty), T_\infty)$ in the upper left (where the two lines cross). Again, we observe how the j.p.d.f. converges to this line as well, forming all together a shape that is similar to a swept wing. With progressing time, the j.p.d.f. contracts towards $(q_{vs}(T_\infty), T_\infty)$.

We note that the temperature of the droplets growing by diffusion in the cloud core is slightly increased within the first large-eddy turnover times, up to times of approximately $t=16$ s or $t\approx 2\,T_{L,B}$. This result of latent heat release competes with the overall mixing to result in the peak of the j.p.d.f. being stretched along the $q_{vs}(T)$ line during the first few eddy turnover times. Interestingly, the small subset of droplets that experiences sudden evaporative cooling at the cloud–clear air interface reach temperatures even lower than those at the dashed line. Their temperature decreases to values as small as $T=290$ K. This is most visible in figure 15(*b*,*c*). Although not shown here, this is a result of a strong evaporative cooling of droplets that fall into regions of dry air due to gravitational settling. In figure 15(*d*) at time $t=32$ s, the tail towards the clear air condition has become well aligned with the dashed line. We also note that the maximum temperature of $T_e=293$ K is consistently not exceeded. This is the initial clear air temperature with lower vapour concentration. All droplets that enter the environment can only shrink and consume heat.

Although not shown here, the same qualitative behaviour follows for TNIb except more slowly in time. Here, again, owing to finite computational resources, we could not run the simulation long enough to approach the final mixing state. Owing to the larger domain size, this state will be reached in TNIb later than in TNIa. Again, the growth process of the droplets and thus the increase of the most probable temperature in the core proceeds for somewhat longer since the supersaturated domain is bigger.

4.4. *Joint Lagrangian statistics of local dissipation rate and local enstrophy*

In order to obtain further quantitative insight on the joint statistics of local enstrophy and kinetic energy dissipation rate fields, we display the j.p.d.f. for TNIa at two different instants in figure 16. In detail, we plot

$$\Pi(\epsilon, \omega^2) = \frac{p(\epsilon, \omega^2)}{p(\epsilon)p(\omega^2)}, \tag{4.1}$$

which normalizes the j.p.d.f. of ϵ and ω^2 by the corresponding single-quantity p.d.f.s in order to highlight the correlation of far tail events better. As the two panels of figure 16 show, particularly very-low- and very-high-amplitude dissipation and local enstrophy events are found in close vicinity to each other. This holds for the whole dynamical evolution of the mixing process and for all runs considered. The bimodal and skewed shape of Π agrees with those of numerical simulations of box turbulence by Schumacher *et al.* (2010) and grid turbulence experiments by Zeff *et al.* (2003). In fluid turbulence, the highest-enstrophy events are generated by vortex stretching. This stretching of a vortex tube always induces strain and thus energy dissipation around the stretched tube as a nonlinear feedback that reduces the original background strain that is responsible for the stretching. This mechanism was studied in detail, for example, in Hamlington, Schumacher & Dahm (2008) and explains why local maxima of dissipation and enstrophy are found in close vicinity.

https://doi.org/10.1017/jfm.2017.23 Published online by Cambridge University Press

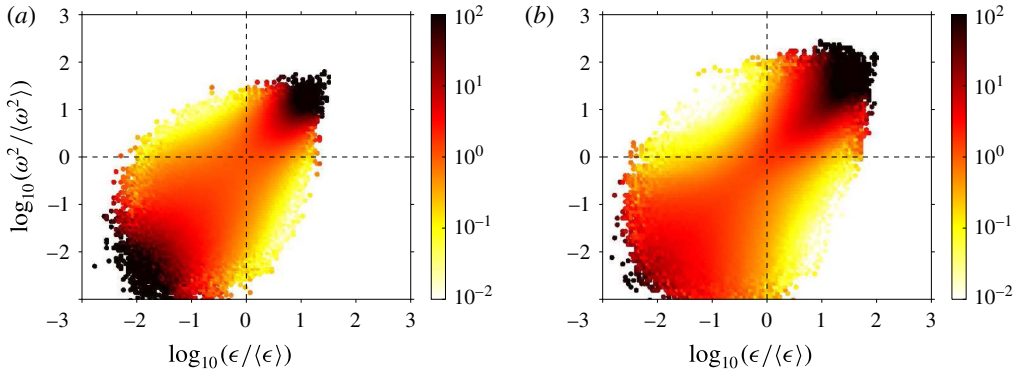


FIGURE 16. (Colour online) Joint p.d.f.s of kinetic energy dissipation rate and local enstrophy for the whole box in the Lagrangian frame of reference: (*a*) $t = 0.5$ s; (*b*) $t = 16$ s. Data are for the TNIa case. Both joint distributions are normalized by the corresponding single-particle p.d.f.s.

5. Summary and outlook

We have presented a DNS study of a shearless mixing layer with phase changes. This simulation set-up reflects some aspects of the entrainment process of unsaturated environmental air into cloudy air as present at the edge of the cloud. At the focus of our DNS study is the interaction of small-scale turbulence and droplet microphysics. Therefore, we modelled the liquid water content as an ensemble of individual water droplets, which are described as collision-free point particles that grow in a supersaturated environment and evaporate in subsaturated air. The thermodynamic conditions are adapted to realistic conditions as present in warm cumulus clouds, and the initial conditions resemble the situation in a decaying cloud with a negative buoyancy inside the cloudy air filament. All simulations are transient processes for the whole evolution time, i.e. they do not reach a statistically steady state. The fluid turbulence is decaying and passes through a transient quasi-steady state. Since all scales of turbulence down to the Kolmogorov length are resolved, the overall domain size is limited and does not exceed 2 m. The present parametric study aims to vary the physical conditions in the mixing evolution with respect to two different aspects: the role of the initial fluid turbulence level outside the cloud filament in comparison to its interior (runs TNIa and TTIa), and the role of the spatial extent of the simulation domain (runs TNIa and TNIb).

When a shearless mixing layer (TNI) is compared with a configuration that has the same TKE inside and outside the cloud filament (TTI), the differences in the dynamical evolution remain small at first glance. This can be seen when global moments in their temporal evolution or the Lagrangian statistics of the droplets are monitored. In TTI the mixing process proceeds faster as quantified by the temporal growth of the mixing layer, $\Delta(t)$. Differences between the two set-ups become more pronounced when higher-order quantities such as production terms of enstrophy and strain are compared. The generation of shear and strain is much stronger when the turbulence levels differ. This suggests that the higher-order quantities are not of primary importance in driving the microphysical response of the condensed phase.

A bigger simulation domain (TNIb) results in a larger flow Reynolds number since the resolution at the smallest scales is the same in all runs. The microphysical

https://doi.org/10.1017/jfm.2017.23 Published online by Cambridge University Press

response in this case differs substantially in two ways. First, mixing proceeds more slowly due to the increase in the large-eddy time. Second, the system is driven towards an increasingly inhomogeneous mixing regime. The latter is generally consistent with recent observations in atmospheric clouds by Beals *et al.* (2015). A general conclusion, therefore, is that the evolution of cloud microphysics during mixing are much more sensitive to large-scale as opposed to small-scale properties of the flow.

As a future extension of the present work, three points should be mentioned. First, we note that our conclusion is for evaporation and condensation, and that growth due to collisions adds greater complexity and therefore could yield a different outcome. A next essential step would therefore be to include other processes such as droplet collisions and coalescence and to investigate the importance of a polydisperse droplet size distribution in the initial droplet ensemble. Secondly, it would be interesting to compare the mixing process as a function of the box size, which will require additional simulations that push the limits of today's computational capabilities. Only a few aspects of the problem have been studied here in order to clearly illustrate the underlying physical processes. Finally, another direction of extending the present work is a study focused on a newly formed rising cloud with a positive buoyancy inside the cloudy fraction.

Acknowledgements

The work of P.G. was supported by the PAKT program of the Leibniz Association (Germany) and the Deutsche Forschungsgemeinschaft by grant no. SCHU 1410/19-1. R.A.S. acknowledges support by the US National Science Foundation. Supercomputing time has been provided at the JUROPA and JURECA supercomputers of the Jülich Supercomputing Centre (Germany) within the projects HIL08 and HIL10 of the John von Neumann Institute for Computing and at the Aaditya HPCS of the Indian Institute of Tropical Meteorology, Pune (India). We wish to thank T. Gotoh, S. Krueger, S. Malinowski, J. P. Mellado, H. Siebert and F. Stratmann for helpful discussions.

REFERENCES

ABMA, D., HEUS, T. & MELLADO, P. J. Direct numerical simulation of evaporative cooling at the lateral boundary of shallow cumulus clouds. *J. Atmos. Sci.* **70**, 2088–2102.

ANDREJCZUK, M., GRABOWSKI, W. W., MALINOWSKI, S. P. & SMOLARKIEWICZ, P. K. 2006 Numerical simulation of cloud–clear air interfacial mixing: effects on cloud microphysics. *J. Atmos. Sci.* **63**, 3204–3225.

ANDREJCZUK, M., GRABOWSKI, W. W., MALINOWSKI, S. P. & SMOLARKIEWICZ, P. K. 2009 Numerical simulation of cloud–clear air interfacial mixing: homogeneous versus inhomogeneous mixing. *J. Atmos. Sci.* **66**, 2493–2500.

ATKINSON, B. W. & ZHANG, J. W. 1996 Mesoscale shallow convection in the atmosphere. *Rev. Geophys.* **34**, 403–431.

AUSTIN, P. H., BAKER, M. B., BLYTH, A. M. & JENSEN, J. B. 1985 Small-scale variability in warm continental cumulus clouds. *J. Atmos. Sci.* **42**, 1123–1138.

BEALS, M. J., FUGAL, J. P., SHAW, R. A., LU, J., SPULER, S. M. & STITH, J. L. 2015 Holographic measurements of inhomogeneous cloud mixing at the centimeter scale. *Science* **350**, 87–90.

BERGOUGNOUX, L., BOUCHET, G., LOPEZ, D. & GUAZZELLI, É. 2014 The motion of solid spherical particles falling in a cellular flow field at low Stokes number. *Phys. Fluids* **26**, 093302.

BLYTH, A. M. 1993 Entrainment in cumulus clouds. *J. Appl. Meteorol.* **32**, 626–641.

BODENSCHATZ, E., MALINOWSKI, S. P., SHAW, R. A. & STRATMANN, F. 2010 Can we understand clouds without turbulence? *Science* **327**, 970–971.

https://doi.org/10.1017/jfm.2017.23 Published online by Cambridge University Press

BRIGGS, D. A., FERZIGER, J. H. & KOSEFF, J. R. 1996 Entrainment in a shear-free turbulent mixing layer. *J. Fluid Mech.* **310**, 215–241.

CROWE, C., SOMMERFELD, M. & TSUJI, Y. 1998 *Multiphase Flows With Droplets and Particles*. CRC Press.

GERASHCHENKO, S., GOOD, G. & WARHAFT, Z. 2011 Entrainment and mixing of water droplets across a shearless turbulent interface with and without gravitational effects. *J. Fluid Mech.* **668**, 293–303.

GERBER, E. H., FRICK, M. G. & JENSEN, J. B. 2008 Entrainment, mixing, and microphysics in trade-wind cumulus. *J. Met. Soc. Japan* **86A**, 87–106.

GILBERT, B. 1980 Diffusion mixing in grid turbulence. *J. Fluid Mech.* **100**, 349–365.

GOOD, G. H., GERASHCHENKO, S. & WARHAFT, Z. 2012 Intermittency and inertial particle entrainment at a turbulent interface: the effect of the large-scale eddies. *J. Fluid Mech.* **694**, 371–398.

GOTOH, T., SUEHIRO, T. & SAITO, I. 2016 Continuous growth of cloud droplets in cumulus cloud. *New J. Phys.* **18**, 043042.

GRABOWSKI, W. W. & WANG, L. P. 2013 Growth of cloud droplets in a turbulent environment. *Annu. Rev. Fluid Mech.* **45**, 293–324.

HAMLINGTON, P. E., SCHUMACHER, J. & DAHM, W. J. A. 2008 Local and nonlocal strain rate fields and vorticity alignment in turbulent flows. *Phys. Rev.* E **77**, 026303.

HEUS, T. & JONKER, H. J. J. 2008 Subsiding shells around shallow cumulus clouds. *J. Atmos. Sci.* **65**, 1003–1018.

HOLZNER, M., LIBERZON, A., NIKITIN, N., LÜTHI, B., KINZELBACH, W. & TSINOBER, A. 2008 A Lagrangian investigation of the small-scale features of turbulent entrainment through particle tracking and direct numerical simulation. *J. Fluid Mech.* **598**, 465–475.

IRELAND, P. J. & COLLINS, L. R. 2012 Direct numerical simulation of inertial particle entrainment in a shearless mixing layer. *J. Fluid Mech.* **704**, 301–332.

KATZWINKEL, J., SIEBERT, H., HEUS, T. & SHAW, R. A. 2014 Measurements of turbulent mixing and subsiding shells in trade wind cumuli. *J. Atmos. Sci.* **71**, 2810–2822.

KNAEPEN, B., DEBLIQUY, O. & CARATI, D. 2004 Direct numerical simulation and large-eddy simulation of a shear-free mixing layer. *J. Fluid Mech.* **514**, 153–172.

KUMAR, B., JANETZKO, F., SCHUMACHER, J. & SHAW, R. A. 2012 Extreme responses of a coupled scalar-particle system during turbulent mixing. *New J. Phys.* **14**, 115020.

KUMAR, B., SCHUMACHER, J. & SHAW, R. A. 2013 Cloud microphysical effects of turbulent mixing and entrainment. *Theor. Comput. Fluid Dyn.* **27**, 361–376.

KUMAR, B., SCHUMACHER, J. & SHAW, R. A. 2014 Lagrangian mixing dynamics at the cloudy–clear air interface. *J. Atmos. Sci.* **71**, 2564–2580.

LANOTTE, S. A., SEMINARA, A. & TOSCHI, F. 2009 Cloud droplet growth by condensation in homogeneous isotropic turbulence. *J. Atmos. Sci.* **66**, 1685–1697.

LEHMANN, K., SIEBERT, H. & SHAW, R. A. 2009 Homogeneous and inhomogeneous mixing in cumulus clouds: dependence on local turbulence structure. *J. Atmos. Sci.* **66**, 3641–3659.

MALINOWSKI, S. P., ANDREJCZUK, M., GRABOWSKI, W. W., KORCZYK, P., KOWALEWSKI, T. A. & SMOLARKIEWICZ, P. K. 2008 Laboratory and modeling studies of cloud–clear air interfacial mixing: anisotropy of small-scale turbulence due to evaporative cooling. *New J. Phys.* **10**, 075020.

MELLADO, J. P. 2010 The evaporatively driven cloud–top mixing layer. *J. Fluid Mech.* **660**, 5–36.

OLIVIERI, S., PICANO, F., SARDINA, G., IUDICONE, D. & BRANDT, L. 2014 The effect of the Basset history force on particle clustering in homogeneous and isotropic turbulence. *Phys. Fluids* **26**, 041704.

ONISHI, R., MATSUDA, K. & TAKAHASHI, K. 2015 Lagrangian tracking simulation of droplet growth in turbulence enhancement of autoconversion rate. *J. Atmos. Sci.* **72**, 2591–2607.

PERRIN, V. E. & JONKER, J. J. H. 2015 Lagrangian droplet dynamics in the subsiding shell of a cloud using direct numerical simulations. *J. Atmos. Sci.* **72**, 4015–4028.

ROGALLO, R. S. 1981 Numerical experiments in homogeneous turbulence. *NASA Tech. Mem.* 81835.

ROGERS, R. R. & YAU, M. K. 1989 *A Short Course in Cloud Physics*. Pergamon.

https://doi.org/10.1017/jfm.2017.23 Published online by Cambridge University Press

SARDINA, G., PICANO, F., BRANDT, L. & CABALLERO, R. 2015 Continuous growth of droplet size variance due to condensation in turbulent clouds. *Phys. Rev. Lett.* **115**, 184501.

SCHUMACHER, J., ECKHARDT, B. & DOERING, C. R. 2010 Extreme vorticity growth in Navier–Stokes turbulence. *Phys. Lett.* A **374**, 861–865.

SCHUMACHER, J., GÖTZFRIED, P. & SCHEEL, J. D. 2015 Enhanced enstrophy generation for turbulent convection in low-Prandtl-number fluids. *Proc. Natl Acad. Sci. USA* **112**, 9530–9535.

SCHUMACHER, J., SREENIVASAN, K. R. & YAKHOT, V. 2007 Asymptotic exponents from low-Reynolds-number flows. *New J. Phys.* **9**, 89.

SHAW, R. A. 2003 Particle turbulence intercations in atmospheric clouds. *Annu. Rev. Fluid Mech.* **35**, 183–227.

SIEBERT, H., BEALS, M., BETHKE, J., BIERWIRTH, E., CONRATH, T., DIECKMANN, K., DITAS, F., EHRLICH, A., FARRELL, D., HARTMANN, S. *et al.* 2013 The fine-scale structure of the trade wind cumuli over Barbados – an introduction to the CARRIBA project. *Atmos. Chem. Phys.* **13**, 10061–10077.

SIEBERT, H., LEHMANN, K., WENDISCH, M., FRANKE, H., MASER, R., SCHELL, D., SAW, E. W. & SHAW, R. A. Probing finescale dynamics and microphysics of clouds with helicopter-borne measurements. *Bull. Am. Meteorol. Soc.* **87** (12), 1727–1738.

DA SILVA, C. B., HUNT, J. C. R., EAMES, I. & WESTERWEEL, J. 2014 Interfacial layers between regions of different turbulence intensity. *Annu. Rev. Fluid Mech.* **46**, 567–590.

STEVENS, B. & BONY, S. 2013 Water in the atmosphere. *Phys. Today* **66** (6), 29–34.

TORDELLA, D. & IOVIENO, M. 2006 Numerical experiments on the intermediate asymptotics of shear-free turbulent transport and diffusion. *J. Fluid Mech.* **549**, 429–441.

TORDELLA, D. & IOVIENO, M. 2011 Small-scale anisotropy in turbulent shearless mixing. *Phys. Rev. Lett.* **107**, 194501.

TOSCHI, F. & BODENSCHATZ, E. 2009 Lagrangian properties of particles in turbulence. *Annu. Rev. Fluid Mech.* **41**, 375–404.

VAILLANCOURT, P. A., YAU, M. K. & GRABOWSKI, W. W. 2001 Microscopic approach to cloud droplet growth by condensation. Part I: model description and results without turbulence. *J. Atmos. Sci.* **58**, 1945–1964.

VEERAVALLI, S. & WARHAFT, Z. 1989 The shearless turbulence mixing layer. *J. Fluid Mech.* **206**, 191–229.

ZEFF, B. W., LANTERMAN, D. D., MCALLISTER, R., ROY, R., KOSTELICH, E. J. & LATHROP, D. P. 2003 Measuring intense rotation and dissipation in turbulent flows. *Nature* **421**, 146–149.

ZONTA, F. & SOLDATI, A. 2014 Effect of temperature-dependent fluid properties on heat transfer in turbulent mixied convection. *Trans. ASME J. Heat Transfer* **136**, 022501.

https://doi.org/10.1017/jfm.2017.23 Published online by Cambridge University Press